

Abstract

29
30
31
32
33
34
35
36
37
38
39
40
41
42
43
44
45
46
47
48

We perform a series of stationary wave model (SWM) experiments in which the boreal summer atmosphere is forced, over a number of locations in the continental U.S., with an idealized diabatic heating anomaly that mimics the atmospheric heating associated with a dry land surface. For localized heating within a large portion of the continental interior, regardless of the specific location of this heating, the spatial pattern of the forced atmospheric circulation anomaly (in terms of 250-mb eddy streamfunction) is largely the same: a high anomaly forms over west-central North America and a low anomaly forms to the east. In supplemental atmospheric general circulation model (AGCM) experiments, we find similar results; imposing soil moisture dryness in the AGCM in different locations within the US interior tends to produce the aforementioned pattern, along with an associated near-surface warming and precipitation deficit in the center of the continent. The SWM-based and AGCM-based patterns generally agree with composites generated using reanalysis and precipitation gauge data. The AGCM experiments also suggest that dry anomalies imposed in the lower Mississippi Valley have remote surface impacts of particularly large spatial extent, and a region along the eastern half of the US-Canada border is particularly sensitive to dry anomalies in a number of remote areas. Overall, the SWM and AGCM experiments support the idea of a positive feedback loop operating over the continent: dry surface conditions in many interior locations lead to changes in atmospheric circulation that act to enhance further the overall dryness of the continental interior.

49 **1. Introduction**

50 From a societal perspective, much of what characterizes the Earth's climate can be
51 related to atmospheric processes – the mean and variability of rainfall in a region, for example,
52 or the statistics of near-surface air temperature. The atmospheric component of climate, with its
53 winds, storms, clouds, and aerosols, along with myriads of other processes, is overwhelmingly
54 complex in and of itself. The full climate system, however, is made even more complex by the
55 interactions of the atmosphere with the system's other components, notably the ocean, the land,
56 and the cryosphere. The coupling of these different components allows, for example, the
57 development and maintenance of modes of behavior, such as the El Nino / Southern Oscillation
58 (ENSO) phenomenon, that otherwise would not exist.

59 While the coupling of the different climate components increases the overall complexity
60 of the system, it also has the beneficial impact of sometimes increasing climate predictability –
61 the ability to predict ahead of time, perhaps weeks to seasons in advance, a climatic variation
62 such as a regional drought. Atmospheric processes are strongly influenced by chaotic
63 atmospheric dynamics. Because of chaos in the atmosphere, forecasts relying solely on
64 atmospheric initialization cannot expect to have skill exceeding about two weeks. Time scales of
65 variation in the ocean, land, and sea ice, however, and of various coupled modes such as ENSO,
66 are much longer, and these longer timescales can translate, through coupling, to predictive skill
67 for various atmospheric quantities. Operational seasonal forecasting systems indeed rely on the
68 added predictability associated with the coupling of the atmosphere to slower components of the
69 system (NRC, 2010).

70 The coupling of the land to the atmosphere potentially allows the long time scales of soil
71 moisture anomalies (weeks to months; Entin et al. 2000; Vinnikov and Yeserkepova 1991) and

72 snow anomalies (winter through the spring melt season) to contribute to atmospheric
73 predictability at these time scales. The idea is simple – if a soil moisture anomaly, for example,
74 is known at the start of a forecast, it can be predicted with some skill weeks to months into the
75 forecast due to the slow time scale over which it varies. If, weeks to months into the forecast, the
76 atmosphere in turn responds in a predictable way to the predicted soil moisture anomaly, then
77 some skill is imparted to atmospheric prediction at these leads. The impacts of soil moisture
78 variations on atmospheric variability have been studied extensively using both climate model
79 analyses (e.g., Delworth and Manabe 1989, Douville and Chauvin 2000, Koster et al. 2006, Guo
80 et al. 2006, Dirmeyer et al. 2013) and observational analyses (e.g., Betts and Ball 1995, Findell
81 and Eltahir 1997, Koster et al. 2003, Taylor et al. 2011). Positive impacts of realistic soil
82 moisture initialization on precipitation and air temperature forecast skill at monthly leads were
83 quantified across a broad range of forecasting systems in the Global Land-Atmosphere Coupling
84 Experiment, Phase 2 (Koster et al. 2011). An impact of snow initialization on forecast skill was
85 demonstrated by Peings et al. (2011) and Ambadan et al. (2015).

86 The present paper focuses specifically on soil moisture anomalies, their impacts on the
87 overlying atmosphere, and their associated impacts on remote precipitation and air temperature
88 fields. The physical mechanisms underlying these impacts are not fully known. A local effect
89 on the air temperature is straightforward; higher soil moisture levels can lead to increased
90 evapotranspiration, which in turn leads to increased evaporative cooling of the land surface and,
91 consequently, of the overlying air (Seneviratne et al. 2010). A local impact on precipitation can
92 also be envisioned: higher soil moistures can increase evapotranspiration and accordingly reduce
93 surface sensible heat flux, leading to a modification of the planetary boundary layer and thus to a
94 modification of conditions determining the onset of moist convection (Betts et al. 1994). To

95 what extent, however, can a soil moisture anomaly affect meteorological conditions in remote
96 locations? On this subject the literature is more limited. For such a remote impact to be
97 predictable – for information at the site of the soil moisture anomaly to be translated to the
98 remote region – atmospheric transports or the atmospheric circulation itself would need to be
99 modified in a predictable way. Douville et al. (2002) suggested that certain soil moisture
100 anomalies may help trigger stationary planetary waves over Europe that in turn may affect the
101 transport of dry air from midlatitudes to the tropics. Lau and Kim (2012) connected extreme
102 weather events in Russia and Pakistan through atmospheric patterns that were potentially
103 amplified by dry land conditions. Koster et al. (2014) showed that forcing an atmospheric
104 general circulation model (AGCM) with a soil moisture dipole over the continental US – wet
105 conditions in the Pacific Northwest and dry conditions in the southern Great Plains – leads to a
106 distinct planetary wave pattern that induces further drying and warming in the latter region.
107 Taylor et al. (2011) demonstrate the impact of surface moisture heterogeneity on the formation
108 of mesoscale circulations that promote storm formation over dry regions. It is worth noting that
109 the impact of other land surface anomalies on the atmospheric circulation and associated remote
110 impacts have also been examined; both Robock et al. (2003) and Cohen et al. (2014), for
111 example, examined the role of Siberian snow cover on the atmospheric circulation and the
112 associated potential for prediction, and Xue et al. (2012) examined the ability of subsurface soil
113 temperature anomalies in the western US to affect conditions in the eastern US via Rossby
114 waves.

115 In the present paper we expand on the findings of Koster et al. (2014) through a more
116 comprehensive analysis of the impacts of North American soil moisture anomalies on the
117 overlying atmospheric circulation and remote meteorological variables, with a focus on boreal

118 summer. Results are shown in the order of the complexity of the models used to produce them.
119 That is, after describing the models and the datasets examined (section 2), we first show a set of
120 results (section 3a) obtained by forcing a relatively simple stationary wave model (SWM) with
121 an idealized heating anomaly that mimics the direct effect of surface drying. The SWM results
122 have the advantage of demonstrating clearly one of our main findings, namely, that the
123 atmospheric circulation responds in a similar way to heating anomalies imposed in very different
124 locations. The SWM results, of course, also have the disadvantage of lacking physical processes
125 and hence the physical complexities of a full AGCM; our second set of results (section 3b) are
126 therefore obtained with a full suite of corresponding AGCM experiments. The AGCM results
127 support the aforementioned main finding, though with the expected increase in noise and with
128 added nuances in the patterns produced. The AGCM experiments also provide information on
129 remote precipitation and air temperature impacts. We then examine available observations-based
130 data (section 3c) and show that they in turn provide support for the SWM and AGCM findings.
131 We conclude (section 3d) with supplemental analyses of the AGCM data that illustrate how the
132 strength of soil moisture-meteorology teleconnections may vary in space.

133 Our AGCM analysis, by the way, utilizes large ensembles (~100-200 members), a
134 reflection of the subtlety of the signals we seek here. We are, in effect, seeking the net impact
135 (e.g., on mean states) of shifts in the probability density functions of various quantities rather
136 than more deterministic relationships that would necessarily lead to a first-order improvement in
137 predictions. This caveat should be kept in mind when evaluating the analyses that follow.

138

139 **2. Models and Datasets Used**

140

141 **a. Stationary Wave Model (SWM)**

142 The nonlinear and time-dependent stationary wave model (SWM) used in this study is
143 based on the three-dimensional primitive equations in σ coordinates. All of the basic variables in
144 the model are deviations from a prescribed zonal mean or 3-D climatological flow. The basic
145 prognostic equations are those for perturbation vorticity, divergence, temperature, and the
146 logarithm of surface pressure. The model-generated transient disturbances are suppressed by
147 applying strong damping. The stationary wave solution is obtained by integrating the model to a
148 quasi-steady state after a short period of time.

149 The model has rhomboidal wavenumber-30 (R30) truncation in the horizontal and 14
150 unevenly spaced σ levels in the vertical. While the R30 resolution (roughly 2.25° latitude \times
151 3.75° longitude) is coarser than that of the AGCM described below (roughly 1° resolution), we
152 nevertheless expect the AGCM and SWM results to be directly comparable. This is because,
153 relative to AGCM results, SWM results are not as affected by resolution. Much of the
154 resolution-dependent behavior in an AGCM stems from its use of model physical
155 parameterizations to produce stationary wave forcings such as diabatic heating. In contrast,
156 diabatic heating in the SWM is prescribed and is thus not resolution-dependent. Output from our
157 R30 SWM experiments and that from SWM experiments at roughly 1° resolution should be
158 similar.

159 The SWM has been shown to be a valuable tool for diagnosing the maintenance of the
160 climatological atmospheric circulation and its anomalies (in terms of magnitude and pattern) as

161 well as for investigating dynamics of stationary waves (e.g., Ting et al. 2001; Held et al. 2002;
162 Schubert et al. 2011). See Ting and Yu (1998) for more details on the SWM.

163

164 **b. Atmospheric General Circulation Model (AGCM)**

165 The simulations examined here were performed with the GEOS-5 (Global Earth
166 Observing System, Version 5) atmospheric general circulation model (AGCM), a component of
167 the state-of-the-art modeling system maintained by the Global Modeling and Assimilation Office
168 (GMAO) of the National Aeronautics and Space Administration's Goddard Space Flight Center
169 (NASA/GSFC). The version of the GEOS-5 AGCM used here is run on a cubed-sphere grid
170 (Putman and Lin 2007). As is standard for this kind of system, unresolvable physical processes
171 are parameterized; GEOS-5 uses the approaches of Moorthi and Suarez (1992) for convection,
172 Bacmeister et al. (2006) for prognostic cloud cover, Chou and Suarez (1994) and Chou
173 (1990,1992) for longwave and shortwave radiation processes, Lock et al. (2000) for turbulence
174 near the surface, and Helfand and Schubert (1995) for the surface layer (though over land the
175 surface layer includes a viscous sublayer). Land surface processes are simulated with the
176 Catchment land surface model (Koster et al. 2000), a model that simulates explicitly the impact
177 of topography-driven subgrid soil moisture variability on the surface energy and water balances.

178 As with all AGCMs, the GEOS-5 AGCM has biases in its simulated climate.
179 Nevertheless, the AGCM is well-vetted. For the past several years, short-term weather forecasts
180 produced by the model have been analyzed extensively by GMAO personnel every week to
181 maintain confidence in model performance and to determine and correct deficiencies; this
182 process ensures the continued maintenance of a state-of-the-art system. The AGCM has been

183 deemed suitable for use in GMAO operations, serving, for example, as the model component of
184 the MERRA and MERRA-2 reanalyses (Modern-Era Retrospective Analysis for Research and
185 Applications; Rienecker et al. 2011; Bosilovich et al. 2016) and, when coupled to an ocean
186 model, as the basis for GMAO seasonal forecasts (Ham et al. 2014). The GEOS-5 AGCM has
187 been used extensively to study the mechanisms underlying climate variability (Schubert et al.
188 2014, Koster et al. 2015, Wang et al. 2016). Molod et al. (2012) document the performance
189 (including biases) of the free-running model, and Gelaro et al. (2014) and Bosilovich et al.
190 (2016) show, respectively, how the model behaves at very high resolution and within an analysis
191 system.

192

193 **c. Observations-Based Data**

194 The SWM and AGCM simulations produce streamfunction fields, and the AGCM also
195 produces near-surface air temperatures and precipitation rates. To evaluate the realism of these
196 model results, we interpret them in the context of available observations-based data.

197 We use reanalysis data to provide observations-based information on soil moisture,
198 streamfunction, and near-surface air temperature. In the MERRA-2 reanalysis (Bosilovich et al.
199 2016), the land surface is forced with precipitation rates that are corrected with gauge-based
200 precipitation observations (Reichle and Liu 2014). As a result, soil moisture contents in the
201 MERRA-2 reanalysis evolve realistically, attaining the level of accuracy seen in traditional Land
202 Data Assimilation System, or LDAS, operational products (e.g., Xia et al 2014). Note that
203 because we utilize MERRA-2 root zone soil moistures only to determine periods for which the
204 real world experienced dry land surface conditions, their level of accuracy should be acceptable;

205 while the products of different LDAS systems do show differences, they nevertheless tend to be
206 highly consistent in their identification of extreme dry periods (e.g., Koster et al. 2009, Wang et
207 al. 2009).

208 We could also use MERRA-2 to provide the observations-based streamfunction and air
209 temperature data we need, but we choose instead to extract these data from the European Centre
210 for Medium-Range Weather Forecasts (ECMWF) ERA-Interim reanalysis (Dee et al. 2011).
211 This choice is driven by the fact that the AGCM experiments described below and the MERRA-
212 2 reanalysis utilize the same atmospheric model, which could potentially promote similar biases
213 in both sets of data. ERA-Interim provides observations-based data that are inherently more
214 independent. (As it turns out, the use of MERRA-2 produces essentially the same results [not
215 shown].) In addition, the near-surface air temperatures produced by ERA-Interim are known to
216 be of high quality (Simmons et al. 2010), probably in part because ERA-Interim uses station
217 measurements of air temperature to update soil temperatures.

218 For precipitation, we use the observations-corrected precipitation output from MERRA-2.
219 Because we only look at precipitation totals for 10-day periods in June and July, the use of the
220 observations-corrected MERRA-2 data is equivalent to using, over land, precipitation data from
221 the Climate Prediction Center (CPC) Unified Gauge-Based Analysis of Global Daily
222 Precipitation (CPCU; ftp://ftp.cpc.ncep.noaa.gov/precip/CPC_UNI_PRCP/GAUGE_GLB/)
223 database and, over the ocean, from a mix of data from the Global Precipitation Climatology
224 Project (GPCP, Adler et al. 2003, Huffman et al. 2009) and the CPC Merged Analysis of
225 Precipitation (CMAP; <ftp://ftp.cpc.ncep.noaa.gov/precip/cmap/>). In essence, then, we compare
226 our AGCM precipitation results over land directly to rain gauge measurements. See Reichle and

227 Liu (2014) for a description of how the different observational precipitation datasets were
228 incorporated into the MERRA-2 data.

229

230 **3. Experiments and Results**

231

232 **a. SWM Responses to Idealized Diabatic Heating Anomalies**

233 In nature, a drier-than-average surface state (i.e., low soil moisture) can affect diabatic
234 heating in the overlying atmosphere through its impact on the surface energy balance – the dry
235 conditions lead to an anomalously high sensible heat flux from the surface and thus to increased
236 near-surface heating in the immediate area of the anomaly. When, in contrast, the surface is
237 anomalously wet and latent heat flux dominates, the associated anomalous diabatic heating may
238 appear geographically far away, depending on where that excess evaporated moisture eventually
239 condenses.

240 To represent the immediate atmospheric impact of a dry surface anomaly and the
241 associated local increase in sensible heat flux, we impose in the SWM, over a selected area of
242 dryness, an idealized diabatic heating anomaly with the vertical profile shown in Figure 1a. The
243 areal extent of the imposed diabatic heating anomaly is given horizontal half-widths of 5°
244 longitude and 5° latitude, as indicated in Figure 1b for one of the experiments. This vertical
245 distribution and spatial extent is consistent with the structures of the diabatic heating anomalies
246 produced in the AGCM experiments described in section 3b below. To illustrate this, the
247 vertical and spatial (zonal) structure of diabatic heating produced in a representative AGCM
248 experiment (specifically, AGCM-L, to be defined below) is illustrated in Figure 1c.

249 In a standard experiment, the anomalous heating is imposed throughout the model
250 integration. The mean basic state used for the SWM is the 3-D June-July averaged climatological
251 (1980-2010) basic flow taken from the GEOS-5 AGCM. The SWM reaches a steady state at
252 about day 25, meaning that results from any day thereafter would represent the steady-state
253 model response. Here we present the model eddy streamfunction solution at day 50.

254 We use this approach in a series of 21 experiments with the SWM, with each experiment
255 assuming a different assumed area of dryness and thus a different geographical placement of the
256 idealized anomaly shown in Figure 1. Figure 2 shows the 21 geographical areas considered. In a
257 given experiment, the imposed idealized anomalous diabatic heating was centered as close as
258 possible (given the grid resolution of the SWM) to the central longitude and latitude of that
259 experiment's indicated area. The 21 SWM experiments are hereafter labeled SWM-A through
260 SWM-U.

261 Figure 3 shows the response of the 250-mb eddy streamfunction field to the imposed
262 heating anomaly in each experiment. Notice the similarity in the responses. In almost all of the
263 experiments, a high anomaly is seen in the west-central part of the northern half of the continent,
264 and in most of the experiments, a low anomaly is seen further to the east. The eddy
265 streamfunction patterns generally look very similar in their placement, though the magnitudes of
266 the responses are substantially reduced when the diabatic heat source is placed on the western
267 coast, and the patterns do change when it is placed toward the eastern coast. Certainly within the
268 continental interior, different placements of the heat source promote a common atmospheric
269 circulation response, with the maximum and minimum of the streamfunction field not simply
270 shifting laterally with the heat source.

271 We choose the following approach to characterize the degree of similarity amongst the
272 responses. We first average the 21 streamfunction anomaly fields in Figure 3 into a single field
273 and then compute the square of the spatial correlation, r^2 , between each experiment's 250-mb
274 streamfunction anomaly field and this average field over the North American area shown. The
275 heavy dashed lines in Figure 4a enclose the nine experiments for which this r^2 is at least 0.65,
276 i.e., for which the average field over the 21 experiments explains about 2/3 or more of the spatial
277 variance of a given experiment's field. Figure 4b then presents the results of a second averaging
278 exercise; it shows the results of averaging the 250-mb streamfunction anomaly fields over the
279 nine experiments indicated in Figure 4a.

280 A comparison of the individual streamfunction anomaly fields in Figure 3 with the
281 pattern in Figure 4b shows that this pattern is indeed a first-order representation of the SWM
282 results for these nine experiments. This point is underlined by Figure 4c, which shows the
283 square of the correlation coefficient between each experiment's streamfunction anomaly field
284 and the 9-experiment average in Figure 4b. Each of the 9 experiments focusing on heating
285 within the delimited area produces a streamfunction field in strong agreement with the 9-
286 experiment average, with r^2 values upward of 0.7.

287 There are presumably many ways to characterize similarity in experiment results. Based
288 on the approach used here, we make the claim that the response of the 250-mb streamfunction
289 field to diabatic heating anywhere within the region delimited in Figure 4a is similar in pattern –
290 regardless of where surface heating is located in this region, the atmospheric circulation responds
291 in much the same way. Much of our later analyses will focus on this interior region.

292

293 **b. AGCM Responses to Imposed Land Surface Dryness**

294 The next step in our analysis is to determine if the basic pattern (Figure 4b) found by the
295 SWM for the interior region in Figure 4a is also found within a full suite of AGCM experiments.
296 We describe the AGCM experiments below.

297

298 *(i) Control Ensemble.* The control for our experiments consists of an ensemble of 768 4-month
299 simulations with the atmosphere and land components of GEOS-5. This decidedly large number
300 of ensemble members helps ensure accurate statistics. Initialization followed the strategy
301 employed by Koster et al. (2014): each simulation was initialized on 1 April 2012, with initial
302 atmosphere and land conditions taken from different years of the MERRA reanalysis, and with
303 the initial atmospheric conditions perturbed slightly to produce multiple ensemble members for
304 each MERRA year. Sea surface temperatures for 2012 (a year for which the real world
305 experienced warming in the Great Plains of the US) were prescribed using Atmospheric Model
306 Intercomparison Study (AMIP)-style protocols (Gates 1992). Each simulation was performed on
307 a C90 cubed-sphere grid (equivalent to $1^\circ \times 1^\circ$ resolution), and output from each simulation was
308 subsequently written out onto a $1^\circ \times 1^\circ$ latitude-longitude grid for analysis.

309

310 *(ii) Experiment Ensembles.* A total of 21 experiments were performed, each experiment
311 consisting of an ensemble of either 96 or 192 simulations that differed from the control only in
312 the prescribed drying of a selected land area. The drying of the selected area proceeded as
313 follows. During every time step from 1 April to 30 June, any precipitation produced over the
314 selected area by the AGCM was artificially zeroed before it reached the land surface, thereby

315 allowing soil moistures in the land model there to evolve to levels corresponding to a 3-month
316 dry period. The artificial zeroing of the precipitation ceased on 1 July, so that during the month
317 of July, soil moistures were allowed to recover. The zeroing of the precipitation during 1 April -
318 30 June was only at the surface; the AGCM's atmospheric vapor and temperature fields, having
319 been modified by condensation processes in the production of precipitation, were not artificially
320 reset to their pre-rainfall values.

321 The 21 areas considered in the AGCM experiments mimic those used for the SWM
322 experiments (see Figure 2), and we will thus refer to the AGCM experiments as AGCM-A
323 through AGCM-U. The regions examined with the AGCM are, in fact, slightly smaller, an
324 artifact of mapping issues associated with our use of a "cube grid" for the AGCM, a grid that
325 does not translate exactly to a latitude-longitude grid. The areas, each roughly of size $7^{\circ} \times 7^{\circ}$,
326 essentially span the continental US. While the individual areas are somewhat smaller than the
327 two examined by Koster et al. (2014), dryness anomalies within them are still able to affect the
328 AGCM's overlying circulation, as will be shown later. The number of ensemble members
329 comprising each experiment is listed in parentheses below the experiment identifier in Figure 2.

330 As in the SWM analysis, experiment results relative to the control are analyzed for the
331 period 1 June - July 31, a time when land surface impacts on the atmosphere are expected to be
332 large due to high surface turbulent fluxes. (We indeed expect land impacts to be reduced during
333 fall through spring, when the turbulent fluxes are reduced due to reduced solar forcing.) In the
334 context of the experimental design, the period examined corresponds to the final month of an
335 extreme 3-month meteorological drought (June) and the first recovery month thereafter (July).
336 Note that while a precipitation deficit was not imposed in the specified area during July,
337 persistence ensured that soil moisture levels there during July remained significantly low. This

338 is illustrated in Figure 5a, which shows the percentile, based on the statistics of the control
339 ensemble, of average July root zone soil moisture content produced by the experiments at each
340 grid cell. The map is in fact a composite of results from the different experiments; percentiles
341 shown within a given area are from the experiment that utilized that area. (High values along
342 some edges, by the way, reflect the aforementioned slight inconsistency between the cube grid
343 and a regular latitude-longitude grid.) July soil moistures tend to lie below the 5th percentile,
344 indicating that soil moistures in the prescribed dryness regions, forced to be dry in June, do
345 indeed remain dry through July. Deserts are an obvious exception, with the percentiles within
346 Region P in particular sometimes strongly (and surprisingly) exceeding 50%; note, however, that
347 these regions feature a very small range of soil moisture in the control, with all control values at
348 the very dry end. The high percentiles in Region P are presumably artifacts, and the high values
349 notwithstanding, July soil moistures in Region P for Experiment P are themselves very low.

350 This last point is emphasized in Figure 5b, which shows the difference in the total
351 evaporation for June and July between each experiment and the control. As in Figure 5a, the
352 map in Figure 5b is a composite; results plotted within a given region are for the experiment
353 focusing on that region (and indeed are derived, for this plot, from the first 96 ensemble
354 members of the experiment). July evaporation rates from Region P in experiment AGCM-P are
355 not significantly increased, despite the percentiles shown for the region in Figure 5a. More
356 broadly, Figure 5b is a useful reference because it indicates the relative strengths of the local
357 diabatic heating anomaly effectively imposed in the different AGCM experiments, given the
358 strong tie between evaporation and sensible heat flux. Whereas the SWM experiments imposed
359 the same diabatic heating anomaly in the different regions, Figure 5b shows that the effective
360 strengths of these anomalies in the AGCM experiments varied across the country, with low

361 values in the western US and northeastern US (e.g., in the neighborhood of the Great Lakes) and
362 with higher values toward the southeast.

363

364 *(iii) Basic Results.* Figure 6 shows the responses of the 250-mb streamfunction, precipitation,
365 and 2-m air temperature fields to the imposed dryness in Region S in Figure 2. (That is, the
366 figure shows the difference between the mean fields for Experiment AGCM-S and the
367 corresponding mean fields for the control.) In the figure, the solid lines, dashed lines, and heavy
368 white lines correspond respectively to differences that are significantly different from zero at the
369 95%, 99%, and 99.9% confidence levels, as determined by a t-test. Clearly seen in Figure 6a is
370 an induced wave pattern in the streamfunction difference field, with a high centered just to the
371 north of the dry area, a low further to the northeast, and another high even further to the
372 northeast, covering the south of Greenland. This wave pattern is clearly evident in the 2-m
373 temperature difference field (Figure 6c) and is also suggested in the precipitation difference field
374 (Figure 6b). In the particularly affected areas to the north and east of Region S, precipitation is
375 reduced by as much as 0.4 mm/day, and temperature is increased by as much as 1K – large
376 differences given the 2-month averaging period. It is worth emphasizing here that, given the
377 design of the experiment, the responses seen in Figure 6 stem solely from localized soil moisture
378 drying in the AGCM – the imposed soil moisture anomalies are indeed having an impact on the
379 atmospheric circulation and on remote near-surface meteorology.

380 Results for all experiments are summarized in Figures 7, 8, and 9. Figure 7 shows the
381 full streamfunction anomalies induced by imposed dryness in the different areas. The anomaly
382 patterns naturally vary among the experiments, far more than they do among the corresponding
383 SWM experiments. This is fully expected given the relative complexity of the AGCM. The

384 differences between the SWM and AGCM experiments in their atmospheric circulation
385 anomalies can be traced to their differences in stationary wave forcing anomalies. Relative to our
386 SWM experiments, which utilize simple, localized diabatic heating anomalies (Figure 1), the
387 AGCM experiments produce more realistic diabatic heating anomalies that vary regionally, and
388 they also (unlike the particular SWM experiments we performed) account for anomalies in
389 transient flux convergences. In addition, unlike the deterministic SWM results, the AGCM
390 results are affected by chaotic atmospheric dynamics, necessitating an averaging over a large
391 number of ensemble members, and even with this averaging, sampling error still has some
392 impact on the AGCM results. Even so, the streamfunction anomalies produced in corresponding
393 AGCM and SWM experiments do agree, at least to first order. Notice, for example, that
394 experiments SWM-F and AGCM-F both produce a similar swath of high values across southern
395 Canada, and experiments SWM-O and AGCM-O both show that dryness on the far east coast
396 locates the high positive streamfunction values relatively far to the east. While the patterns
397 produced in experiments SWM-P and AGCM-P and in SWM-Q and AGCM-Q differ
398 significantly, this difference can be traced to the fact that in the AGCM, the zeroing of the
399 rainfall in these regions did not lead to a large reduction in surface latent heat flux (and thus to a
400 large increase in the heating of the overlying air through enhanced surface sensible heat flux),
401 since soil moistures in the control simulations were already dry in these regions during the
402 months considered (see Figure 5b). The SWM and AGCM experiments were thus fundamentally
403 different for both of these regions.

404 Consider now the experiments for which dryness is imposed within the area demarcated
405 in Figure 4a (AGCM-B,C,D,K,L,M,R,S,T; the associated experimental results are enclosed
406 within the red solid line in Figure 7). An interesting feature seen for all of these experiments is

407 the production of a high (with experiment-dependent magnitude) over the western-central US
408 and the corresponding production of a low that straddles the northeastern coast. Though the
409 details differ (again, the AGCM is much more complex than the SWM, and the AGCM results
410 shown here are affected somewhat by sampling), the basic first-order pattern produced by an
411 imposed land surface dryness in the interior region is quite similar to that found for the SWM.
412 (This will be demonstrated further in section 3c below; averaging the precipitation changes
413 produced by the AGCM experiments that focus on the demarcated interior region produces a
414 field very similar to that shown in Figure 4b for the SWM experiments.) In other words, the
415 AGCM results support, certainly to first order, the idea that dry conditions anywhere within the
416 demarcated interior region produce a common atmospheric circulation response.

417 Beyond providing information on atmospheric circulation, the AGCM experiments are
418 particularly interesting because they provide information on precipitation and near-surface air
419 temperature response to the imposed dryness anomalies – they provide, in particular, some
420 indication of how surface dryness can affect remote near-surface meteorology. Such remote
421 impacts are examined further in section 3d. For now, consider Figure 8, which shows the
422 precipitation anomalies produced in the different AGCM experiments. To some degree, several
423 of the experiments in the demarcated interior continental region produce similar precipitation
424 reductions in southern Canada and in the eastern half of the US, down to the Gulf of Mexico
425 (with details, of course, differing with experiment). Some similarities in precipitation response
426 would indeed be expected from the aforementioned similar response in the streamfunction field,
427 given that specific changes in large-scale atmospheric circulation can induce specific changes in
428 precipitation.

429 Figure 9 shows the 2-meter air temperature anomalies produced in the AGCM
430 experiments. With a few exceptions (namely, I, J, P, and Q – desert regions, for which the
431 zeroing of precipitation did not strongly affect the soil moisture), the impact of the imposed
432 drying is locally very strong, as might be expected given the associated reduced level of local
433 evaporative cooling (Figure 5b). Many experiments, however, show in addition a remote air
434 temperature impact. Several of the experiments focusing on dryness in the demarcated region in
435 Figure 4a show warming along a swath extending from north-central North America to the Gulf
436 of Mexico, a similarity that may stem from the aforementioned similarity in the streamfunction
437 response.

438

439 **c. Signals Inherent in Observations-Based Data**

440 The results in section 3b relate to the AGCM's inherent climate. While the hope is that
441 they also represent nature, this is, of course, far from guaranteed. Unfortunately, verifying
442 definitively our results with observations is made impossible by the limited extent of available
443 observations-based data. To a large extent the shifts examined in the experiments above are
444 subtle; given the large number of simulations constituting our ensembles, we are effectively
445 examining here the net impact of shifts in probability distribution functions (PDFs). Reanalyses,
446 which typically cover less than 40 years, are inadequate for a proper analysis of PDF shifts.
447 Another key difficulty is the fact that when soil moisture in nature is dry in, say, region K of
448 Figure 2, it also tends to be anomalously dry elsewhere (say, in region L and M), complicating
449 tremendously the isolation of specific impacts associated with region K's dryness.

450 The analyses above, however, suggest a way of addressing at least the second difficulty.
451 Despite the spatial shifts in the local diabatic heating induced by the different dryness regions in
452 Figure 2, the atmosphere in the different SWM and AGCM experiments responds in a similar
453 way – dry conditions (or diabatic atmospheric heating associated with dry conditions) in the
454 interior of the US tend to produce a similar streamfunction anomaly pattern. A possible
455 inference from this result is that in the complex set of available observations, the key feature to
456 look for is not a soil moisture deficit in a specific region but an average dryness in a large
457 continental region (namely, that delimited in Figure 4a), without regard to the spatial distribution
458 of this dryness – where it is maximized, where it is small, etc. If the SWM and AGCM results
459 are valid, then the atmosphere should tend to show the same response to overall continental
460 dryness regardless of the specific spatial pattern.

461 With this in mind, we now analyze observations-based 250-mb stream function,
462 precipitation, and air temperature fields associated with continental-scale antecedent land surface
463 dryness.

464
465 *(i) Compositing strategy.* We use a compositing approach to draw out signals, if they exist, in
466 the observations-based data. Within each year of 1980-2014, we consider six 10-day periods:
467 June 1-10, June 11-20, June 21-30, July 1-10, July 11-20, and July 21-30, amounting to a total of
468 210 10-day periods. We tie to each period an antecedent soil moisture index in the following
469 way. First, we standardize, on a daily basis, the MERRA-2 root zone soil moisture within each
470 grid cell of the interior region demarcated in Figure 4a. Then, for the 10-day period in question,
471 we identify the date falling fifteen days prior to the start of the period and compute, for that day,
472 the average of the standardized soil moisture values across the region. A large negative value for

473 this average implies that, on average, the large-scale continental region was generally very dry
474 15 days prior to the period in question. (See section 2c for a discussion of the realism of
475 MERRA-2 soil moisture values.) We use soil moistures at a 15-day lead rather than concurrent
476 soil moistures to help ensure that the soil moisture signals on which we base our composites are
477 not simply a passive reflection of the meteorology we are examining. Fifteen days lies above the
478 typical time scales of planetary wave development and maintenance in response to local heating
479 anomalies.

480 Our composites are based on the driest 10% of antecedent average soil moisture values.
481 From the 210 June-July decads examined, we thus compute the average 250-mb stream function,
482 precipitation, and air temperature anomaly fields over the 21 driest cases.

483

484 *(ii) Results.* Figure 10a, 10b, and 10c show respectively the resulting composites of 250-mb
485 streamfunction (from ERA-Interim), precipitation (from CPCU, via MERRA-2), and 2-m air
486 temperature (from ERA-Interim). The composited full streamfunction field shows a high along
487 the U.S.-Canada border in the central part of the continent. The composited precipitation field
488 shows a reduction of precipitation along the eastern border of the demarcated interior region
489 along with some increases in precipitation in various surrounding areas, and the composited
490 temperature field shows a positive temperature anomaly that spans much of the interior region.

491 For comparison, Figure 10d shows the corresponding streamfunction anomaly field from
492 the SWM experiments – it shows the sum of the fields obtained in the experiments imposing
493 diabatic heating anomalies within the indicated region. The positioning of the positive
494 streamfunction lobe from the observational composite agrees to first order with that in the SWM

495 results. While the observational composite is largely missing the negative lobe in the east, the
496 square of the spatial correlation coefficient between the patterns in Figures 10a and 10d over the
497 full area of each panel is reasonably high ($r^2=0.36$).

498 Finally, Figures 10e, 10f, and 10g show the corresponding fields derived from the AGCM
499 experiments. To construct the figures, we simply add together the June-July anomalies of the
500 experiments corresponding to the areas delimited by the heavy black lines, making the
501 assumption (as we did above for the SWM) that, in the AGCM, the effects of the different
502 dryness areas on continental meteorology combine linearly. (This assumption is strongly
503 supported by the results of Koster et al. [2014]; see their Figure 5.) In comparing the
504 observational composites and the AGCM results, the first thing to note is the difference in scale.
505 This said, notice that the *patterns* inherent in the observational composites and the AGCM
506 results are again similar. Only slight spatial shifts, for example, are seen in the positions of the
507 large precipitation and air temperature anomalies.

508 We emphasize here that these results do not prove that the SWM and AGCM experiments
509 properly represent nature. Again, the experiments address the net impact of shifts in the
510 underlying PDFs of the meteorological fields, shifts that cannot be captured by the limited
511 observational record. That is, even if the model results represented nature perfectly (which,
512 given their inherent biases, they presumably do not), we would still expect to see differences
513 between the observational and model results. Nevertheless, the comparisons in Figure 10 are
514 promising; they show that the experimental results are at least consistent with available
515 observations.

516

517 **d. Additional Findings Regarding Remote Land Surface Impacts**

518 The similarity in the pattern of the atmospheric response to dryness in different parts of
519 the North American continent is the main result of this study. Nevertheless, the AGCM
520 experiments hold a wealth of information that can be tapped for further understanding of land-
521 atmosphere interactions. Here, we distill the extensive amount of information in Figures 7-9 into
522 two simple aggregate quantities, quantities that together characterize the first-order impact of soil
523 moisture anomalies on meteorological variables in remote locations and how this impact varies
524 with location.

525 The first aggregate quantity, the “impact extent”, measures the spatial extent of the
526 impact of each imposed dryness region in Figure 2. While it is related in concept to more
527 sophisticated diagnostics described in the literature for characterizing the remote reach of
528 localized anomalies (e.g., the climate sensitivity maps constructed by Barsugli et al. (2006) from
529 the results of SST warm patch experiments), the diagnostic we use here is more limited, focusing
530 only on the spatial extent of this reach rather than on the amplitude of the response. Our quantity
531 is computed as follows. For a given experiment, and for a given meteorological variable
532 (precipitation or air temperature), we count the number of $1^\circ \times 1^\circ$ grid cells in North America (at
533 least the part of North America shown in Figure 11) for which the change in the meteorological
534 variable determined for the experiment was significantly different from zero at the 99%
535 confidence level or higher, according to a t-test. This number, which indeed reflects the area
536 within the dashed contours in Figures 8 and 9, is then plotted in Figure 11 – the number
537 computed for a given experiment is plotted within the corresponding imposed dryness area for
538 that experiment.

539 Figure 11a shows that for precipitation, the impact extent is highest for the dryness
540 regions encompassing the Gulf Coast and parts of the Mississippi Valley (regions M, N, S, T).
541 When these areas are forced to be dry, the remote (plus local) impacts of the dryness are felt
542 across a relatively large area. High values also appear in an area around Montana (regions B and
543 C). Values along either coast are relatively small, meaning that when these areas are dry, the
544 spatial extent of the resulting impact on precipitation is slight. In fact, as might be expected, the
545 impact extent varies to some degree with the impact of the drying on the June-July evaporation
546 rates (Figure 5b). (Note that a 99% confidence level suggests that roughly 1%, or 36, of the
547 3621 grid cells considered here will be falsely labeled significant. Values below 48 in the plots
548 are shaded gray, suggesting little or no impact.)

549 For air temperature (Figure 11b), region S has the greatest impact extent, followed by
550 region B. Aside from region O, dryness regions along either coast again have minimal or no
551 impact. Curiously, for some experiments, spatial impacts on air temperature appear smaller than
552 those on precipitation, despite the fact that for air temperature, a local impact at the very least is
553 almost guaranteed due to a reduction in local evaporative cooling.

554 The second aggregate quantity, the “sensitivity to remote dryness”, measures the degree
555 to which a given grid cell is affected by soil moisture anomalies in different regions. This
556 sensitivity is computed at each grid cell as the number of different experiments for which a
557 meteorological quantity (precipitation or air temperature) at the grid cell was modified at a
558 significance level of 99% or higher, according to a t-test. Figure 12a shows the spatial
559 distribution of the sensitivity for precipitation. Notice that 4 to 6 distinct dryness areas are able
560 to affect the June-July precipitation in various grid cells along the eastern half of the US-Canada
561 border; by this measure, these grid cells are particularly susceptible to remote effects. In general,

562 the eastern half of the US is more sensitive to US soil moisture dryness than the western half.
563 The corresponding plot for air temperature (Figure 12b) also shows an east-west contrast but
564 locates the region of highest “sensitivity to remote dryness” along the southeastern coast. Of
565 course, it is important to keep in mind that the patterns in Figure 12 are determined, to some
566 degree, by the distribution of dryness regions in Figure 2. If we had examined additional
567 experiments with imposed dryness in Canada and Mexico, the patterns in Figure 12 would
568 presumably be modified, particularly in or near these outside regions.

569 The quantities plotted in Figures 11 and 12 are, in some ways, converses of each other;
570 Figure 11 in essence shows the strength (local plus remote) of a “source” of meteorological
571 anomalies, and Figure 12 shows, in a way, the strength of their “sink”. The locations of the
572 sources and sinks are different, underlining the geographical connections that exist between land
573 areas through the overlying circulation and its sensitivity to surface processes.

574

575 **4. Summary and Discussion**

576 The simulations with the stationary wave model (SWM) suggest that when a diabatic
577 heating anomaly is imposed in the interior of the continental US (anywhere within the delimited
578 area in Figure 4a) during boreal summer, the atmospheric circulation responds in a very similar
579 way: it produces a positive eddy streamfunction anomaly in the west-central part of the
580 continent and a negative anomaly to the east. This basic response is also seen, at least to first
581 order, in AGCM experiments when soil moisture contents in different parts of the continental
582 interior are forced to be dry. The AGCM experiments further allow us to identify impacts of the
583 imposed soil moisture dryness on remote near-surface meteorological fields. As indicated by the

584 averages in the right-hand column of Figure 10, dry soil moistures in the interior continental
585 region tend to produce warm conditions within the region (Figure 10g) and reduced rainfall a
586 little to the east (Figure 10f). Observational composites (Figures 10a-c) are consistent, again to
587 first order, with the modeled impacts. (It is worth emphasizing again that all of these results are
588 for June-July only; land dryness impacts may be reduced during non-summer months due to
589 reductions in surface turbulent fluxes associated with reduced solar forcing.)

590 The overall behavior established in our experiments is strongly suggestive of a positive
591 feedback loop, as captured in the schematic in Figure 13: dry conditions within the continental
592 interior lead to changes in the atmospheric circulation that in turn lead to further warming and
593 drying there. Consider, for example, the results of imposing soil moisture dryness in region L of
594 Figure 1. According to Figure 7l, this leads to a 250-mb streamfunction high over region L that
595 also extends further to the north. Figures 8l and 9l show that this in turn leads to a warm and dry
596 anomaly just north of the region – conditions that, according to experiment AGCM-D, should
597 lead to additional warming and drying in the area (Figures 8d and 9d). The positive feedback
598 loop outlined in Figure 13 may have impacts on the spatial extent of drought, helping a local dry
599 anomaly in, say, Kansas and Nebraska spread spatially across the continental interior. The
600 mechanics of this feedback loop are worthy of further study.

601 What are the mechanisms by which an atmospheric circulation anomaly translates to
602 anomalies in surface air temperature and precipitation? At these latitudes, streamfunction
603 anomalies and geopotential height anomalies are largely coincident, and as discussed in Koster et
604 al. (2014), an upper-level positive height anomaly can affect surface temperature through an
605 associated increase in subsidence, which promotes cloudless skies and thereby an increased
606 amount of incoming solar radiation reaching the surface. Lower level circulation changes,

607 however, are undoubtedly also important, as they can lead to precipitation anomalies through
608 changing atmospheric moisture transport and convergence in the lower troposphere. We should
609 note that the lower level impacts amongst the experiments are less systematic. Anomalies in
610 850mb wind circulation patterns (not shown), as generated by the different AGCM experiments,
611 do not show the level of agreement seen in Figure 7 largely because the anomalies are of smaller
612 spatial extent and tend to be more centered over the individual imposed dryness regions. This
613 said, however, some agreement in the 850mb wind response is seen, and supplemental analyses
614 of the AGCM results indicate that the west-central North America streamfunction anomaly
615 produced in most of our experiments does tend to tilt westward with height. This westward tilt
616 may explain why the precipitation anomalies produced in our AGCM experiments tend to lie
617 slightly eastward of the air temperature anomalies (compare Figures 10f,g), given that
618 precipitation deficits are largely maintained by reduced atmospheric moisture flux convergences
619 due to changes in low-level atmospheric circulation (e.g., Wang et al 2010; Wang and Schubert
620 2014). Meanwhile, changes in low-level winds bring, in some cases, warm air in from the south,
621 further increasing temperature (not shown). A full understanding of the mechanisms linking the
622 3-D circulation patterns to surface anomalies needs additional study through focused
623 experimentation and associated budget analysis for surface energy, air temperature and
624 atmospheric moisture.

625 While the feedback loop outlined in Figure 13 is intriguing, we must emphasize again a
626 critical aspect of our results, namely, the need for large ensembles (96-192 members) to draw out
627 the indicated patterns in Figures 7-9. The size of these ensembles speaks to the weakness of the
628 model atmosphere's response to the imposed surface anomalies; as noted above, our experiments
629 effectively address shifts in the PDFs of atmospheric response. Dry conditions for a given year

630 in the central US will not necessarily lead to the indicated streamfunction anomalies during that
631 year and an associated strengthening of the dry anomaly; all we can claim is an increased
632 likelihood for this to happen.

633 In other words, the feedback's operation in the AGCM is probabilistic. It is presumably
634 probabilistic in nature as well. The fact that the magnitudes of the responses in Figure 10 are
635 larger for the observational composites than for the model results (while the patterns are roughly
636 the same) in fact may suggest that the feedback in the model is weaker than it is in nature.
637 Additional work is needed to learn if this is true and whether the feedback is indeed large enough
638 in nature to be useful for, say, forecast applications.

639 Perhaps most intriguing of all is our finding, through both the SWM and AGCM
640 analyses, that the atmospheric circulation responds in such a consistent way to surface heating
641 anomalies regardless of the specific geographical positioning of these anomalies within the
642 continental interior (Figures 3 and 7). We are currently performing analyses aimed at explaining
643 this marked similarity in response and the relatively reduced response produced when the dry
644 anomalies are near the western or eastern coast.

645

646 Acknowledgments. Support for this project was provided by the NOAA Modeling, Analysis,
647 Predictions and Projections (MAPP) program; the NASA Energy and Water Cycle Study
648 (NEWS) program; and the NASA Modeling, Analysis, and Prediction Program.

649

650

References

651
652
653
654
655
656
657
658
659
660
661
662
663
664
665
666
667
668
669
670
671

Adler, R. F., and Coauthors, 2003: The Version-2 Global Precipitation Climatology Project (GPCP) monthly precipitation analysis (1979–present). *J. Hydrometeor.*, 4, 1147–1167, doi:10.1175/1525-7541.

Ambadan, J. T., A. A. Bert, and W. J. Merryfield, 2015: Influence of snow and soil moisture initialization on sub-seasonal predictability and forecast skill in boreal spring. *Clim. Dyn.*, doi 10.1007/s00382-015-2821-9.

Bacmeister, J. T., M. J. Suarez, and F. R. Robertson, 2006: Rain reevaporation, boundary layer convection interactions, and Pacific rainfall patterns in a AGCM. *J. Atmos. Sci.*, 63, 3383-3403.

Barsugli, J. J., S.-I. Shin, and P. D. Sardeshmukh, 2006: Sensitivity of global warming to the pattern of tropical ocean warming. *Clim. Dyn.*, 27, 483-492.

Betts, A. K., and J. H. Ball, 1995: The FIFE surface diurnal cycle climate. *J. Geophys. Res.*, 100, 25679-25693.

Betts, A.K., J.H. Ball, A.C.M. Beljaars, M.J. Miller, and P. Viterbo, 1994: Coupling between land-surface, boundary-layer parameterizations and rainfall on local and regional scales: Lessons from the wet summer of 1993. Preprints, Fifth Conf. on Global Change Studies, 74th Annual Meeting, Nashville, TN, Amer. Meteor. Soc.

Bosilovich, M. and Co-Authors, 2016: MERRA-2, Initial Evaluation of the Climate. Tech. Rep. Ser. on Global Modeling and Data Assimilation, 43, NASA/TM-2012-104606, 139 pp.

672 Chou, M.-D., 1990: Parameterizations for the absorption of solar radiation by O₂ and CO₂ with
673 applications to climate studies. *J. Climate*, 3, 209-217.

674 Chou, M.-D., 1992: A solar radiation model for use in climate studies. *J. Atmos. Sci.*, 49, 762-
675 772.

676 Chou, M. -D., and M.J. Suarez, 1994: An efficient thermal infrared radiation parameterization
677 for use in general circulation models, NASA Tech. Memorandum 104606-Vol 3, NASA,
678 Goddard Space Flight Center, Greenbelt, MD.

679 Cohen, J., J. C. Furtado, J. Jones, M. Barlow, D. Whittleston, and D. Entekhabi, 2014: Linking
680 Siberian snow cover to precursors of stratospheric variability. *J. Climate*, 27, 5422-5432.

681 Dee, D. P., and Coauthors, 2011: The ERA-Interim reanalysis: Configuration and performance
682 of the data assimilation system. *Quart. J. Roy. Meteor. Soc.*, 137, 553–597,
683 doi:10.1002/qj.828.

684 Delworth, T.L., and S. Manabe, 1989: The influence of soil wetness on near-surface
685 atmospheric variability. *J. Clim.*, 2, 1447-1462.

686 Dirmeyer, P. A., S. Kumar, M. J. Fennessy, E. L. Altshuler, T. DelSole, Z. C. Guo, B. A. Cash,
687 and D. Straus, 2013: Model estimates of land-driven predictability in a changing climate
688 from CCSM4. *J. Climate*, 26, 8495-8512.

689 Douville, H., and F. Chauvin, 2000: Relevance of soil moisture for seasonal climate predictions,
690 A preliminary study. *Clim. Dyn.*, 16, 719-736.

691 Douville, H., 2002: Influence of soil moisture on the Asian and African monsoons. Part II:
692 Interannual variability. *J. Climate*, 15, 701–720.

693 Entin, J. K., A. Robock, K. Y. Vinnikov, S. E. Hollinger, S. Liu, and A. Namkhai, 2000:
694 Temporal and spatial scales of observed soil moisture variations in the extratropics. *J.*
695 *Geophys. Res.*, **105**, 11865–11877.

696 Findell, K. L., and E. A. B. Eltahir, 1997: An analysis of the soil moisture-rainfall feedback,
697 based on direct observations from Illinois. *Water Resour. Res.*, **33**, 725-735.

698 Gelaro, R. and Co-Authors, 2015: Evaluation of the 7-km GEOS-5 Nature Run. Tech. Rep. Ser.
699 on Global Modeling and Data Assimilation, 36, NASA/TM-2012-104606, 285 pp.

700 Guo, Z., and 25 others, 2006: GLACE, The global land-atmosphere coupling experiment, 2,
701 Analysis. *J. Hydrometeorology*, **7**, 611-625.

702 Ham, Y.-G., S. D. Schubert, Y. Vikhliav, and M. J. Suarez, 2014: An assessment of the ENSO
703 forecast skill of the GEOS-5 system. *Climate Dynamics*, doi 10.1007/s0-0382-014-2063-
704 2.

705 Helfand, H. M., M. and S. D. Schubert, 1995: Climatology of the Simulated Great Plains Low-
706 Level Jet and Its contribution to the Continental Moisture Budget of the United States. *J.*
707 *Climate*, **8**, 784-806.

708 Huffman, G. J., R. F. Adler, D. T. Bolvin, and G. Gu, 2009: Improving the global precipitation
709 record: GPCP version 2.1. *Geophys. Res. Lett.*, **36**, L17808, doi:10.1029/2009GL040000.

710 Koster, R. D., M. J. Suarez, A. Ducharne, M. Stieglitz, and P. Kumar, 2000: A catchment-based
711 approach to modeling land surface processes in a general circulation model: 1. Model
712 structure, *J. Geophys. Res.*, **105**(20), 24,809– 24,822.

713 Koster, R. D., M. J. Suarez, R. W. Higgins, and H. M. Van den Dool, 2003: Observational
714 evidence that soil moisture variations affect precipitation. *Geophys. Res. Lett.*, **30**,
715 doi:10.1029/2002GL016571.

716 Koster, R. D., Z. Guo, P. Dirmeyer, and 23 others, 2006: GLACE, The global land-atmosphere
717 coupling experiment, 1, Overview. *J. Hydrometeor.*, **7**, 590-610.

718 Koster, R. D., Z. Guo, R. Yang, P. A. Dirmeyer, K. Mitchell, and M. J. Puma, 2009: On the
719 nature of soil moisture in land surface models. *J. Climate*, **22**, 4322-4335.

720 Koster, R. D., and Co-authors, 2011: The second phase of the Global Land-Atmosphere
721 Coupling Experiment, Soil moisture contributions to subseasonal forecast skill. *J.*
722 *Hydromet.*, **12**, 805-822.

723 Koster, R. D., Y. Chang, and S. D. Schubert, 2014: A mechanism for land-atmosphere feedback
724 involving planetary wave structures. *J. Climate*, **27**, 9290-9301.

725 Lau, W. K., M., and K.-M. Kim, 2012: The 2010 Pakistan flood and Russian heat wave,
726 Teleconnection of hydrometeorological extremes. *J. Hydromet.*, **13**, 392-403.

727 Lock, A. P., A. R. Brown, M. R. Bush, G. M. Martin, and R. N. B. Smith, 2000: A new boundary
728 layer mixing scheme. Part I: Scheme description and single-column model tests. *Mon.*
729 *Wea. Rev.*, **138**, 3187-3199.

730 Molod, A., L. Takacs, M. Suarez, J. Bacmeister, I.-S. Song, and A. Eichmann, 2012: The GEOS-
731 5 atmospheric general circulation model, Mean climate and development from MERRA
732 to Fortuna. *Tech. Rep. Ser. on Global Modeling and Data Assimilation*, **28**, NASA/TM-
733 2012-104606, 115 pp.

734 Moorthi, S., and M. J. Suarez, 1992: Relaxed Arakawa Schubert: A parameterization of moist
735 convection for general circulation models. *Mon. Wea. Rev.*, 120, 978-1002.

736 National Research Council, 2010: Assessment of intraseasonal to interannual climate prediction
737 and predictability. The National Academies Press, Washington, D.C, 181 pp.

738 Peings, Y., H. Douville, R. Alkama, and B. Decharme, 2011: Snow contribution to springtime
739 atmospheric predictability over the second half of the twentieth century. *Clim. Dyn.*, 37,
740 985-1004.

741 Putman, W. M., and S.-J. Lin, 2007: Finite-volume transport on various cubed-sphere grids.
742 *Journal of Computational Physics*, 227 (1): 55-78.

743 Reichle, R. H., and Q. Liu, 2014: Observation-corrected precipitation estimates in GEOS-5.
744 Tech. Rep. Ser. on Global Modeling and Data Assimilation, 35, NASA/TM-2012-
745 104606, 18 pp.

746 Rienecker, M. M., and Co-Authors, 2011: MERRA, NASA's Modern-Era Retrospective
747 Analysis for Research and Applications. *J. Climate*, **24**, 3624-3648.

748 Robock, A., M. Mu, K. Vinnikov, and D. Robinson, 2003: Land surface conditions over Eurasia
749 and Indian summer monsoon rainfall. *J. Geophys. Res.*, 108, D4, 4131,
750 doi:10.1029/2002JD002286.

751 Schubert, S. D., H. Wang, R. D. Koster, and M. J. Suarez, 2014: Norther Eurasian heat waves
752 and droughts. *J. Climate*, 27, 3169-3207.

753 Seneviratne, S. I., T. Corti, E. L. Davin, M. Hirschi, E. B. Jaeger, I. Lehner, B. Orlowsky, and A.
754 J. Teuling, 2010: Investigating soil moisture–climate interactions in a changing climate:
755 A review. *Earth Sci. Rev.*, **99**, 125–161, doi:10.1016/j.earscirev.2010.02.004.

756 Simmons, A. J., K. M. Willett, P. D. Jones, P. W. Thorne, and D. P. Dee, 2010: Low-frequency
757 variations in surface atmospheric humidity, temperature, and precipitation: Inferences
758 from reanalyses and monthly gridded observational data sets. *J. Geophys. Res.*, **115**,
759 D01110, doi:10.1029/2009JD012442.

760 Taylor, C. T., A. Gounou, F. Guichard, P. P. Harris, R. J. Ellis, F. Couvreux, and M. De Kauwe,
761 2011: Frequency of Sahelian storm initiation enhanced over mesoscale soil-moisture
762 patterns. *Nature Geosci.*, **4**, 430–433.

763 Vinnikov, K. Ya., and I. B. Yesserkepova, 1991: Soil moisture: Empirical data and model results.
764 *J. Climate*, **4**, 66–79.

765 Wang, A., T. J. Bohn, S. P. Mahanama, R. D. Koster, and D. P. Lettenmaier, 2009: Multimodel
766 ensemble reconstruction of drought over the continental United States. *J. Climate*, **22**,
767 2694–2712.

768 Wang, H., S. D. Schubert, M. J. Suarez, and R. D. Koster, 2010: The Physical Mechanisms by
769 Which the Leading Patterns of SST Variability Impact U.S. Precipitation. *J. Climate*, **23**,
770 1815–1836.

771 Wang, H., and S. D. Schubert, 2014: The Precipitation Response over the Continental United
772 States to Cold Tropical Pacific Sea Surface Temperatures. *J. Climate*, **27**, 5036–5055.

773 Wang, H., S. D. Schubert, and R. D. Koster, 2016: The role of stationary Rossby waves in the
774 development of drought over North America and links to northern Eurasia. Chapter in
775 Patterns of Climate Extremes: Trends and Mechanisms, Eds. Wang, S.-Y., Jin-Ho Yoon,
776 Chris Funk, and R. R. Gillies, ISBN: 978-1-119-06784-9. In press.

777 Xia, Y., and Coauthors, 2012: Continental-scale water and energy flux analysis and validation
778 for the North American Land Data Assimilation System project phase 2 (NLDAS-2): 1.
779 Intercomparison and application of model products. *J. Geophys. Res.*, 117, D03109,
780 doi:10.1029/2011JD016048.

781 Xue, Y., R. Vasic, Z. Janjic, Y. M. Liu, and P. C. Chu, 2012: The impact of spring subsurface
782 soil temperature anomaly in the western U.S. on North American summer precipitation:
783 A case study using regional climate model downscaling. *J. Geophys. Res.*, 117, D11103,
784 doi:10.1029/2012JD017692.

785

List of Figures

786

787 Figure 1. a. Vertical profile of idealized diabatic heating anomaly imposed in the SWM
788 atmosphere over a selected geographical area. b. Spatial distribution of imposed
789 idealized heating anomaly near the ground surface ($\sigma = 0.9966$), for experiment SWM-L.
790 c. Vertical and zonal structure of the ensemble mean June-July diabatic heating
791 anomalies produced in Experiment AGCM-L, averaged between 37°N and 44°N. Units:
792 K/day.

793 Figure 2. Areas of imposed dryness considered in the 21 SWM and AGCM experiments (labeled
794 A through U). In a given AGCM experiment, the indicated region was forced to be dry
795 through the artificial zeroing of the incident precipitation in April through June. The
796 number of AGCM ensemble members associated with each experiment is indicated in
797 parentheses.

798 Figure 3. Eddy streamfunction anomaly fields at 250 mb produced in the SWM experiments.
799 The boxes indicate the locations for which the idealized diabatic heating source is placed.

800 Figure 4. Indication of the similarity between the 250-mb eddy streamfunction responses in the
801 different SWM experiments. a. Location of the 9 experimental regions for which the
802 square of the spatial correlation between the experiment's 250-mb eddy streamfunction
803 field and the average field over all 21 experiments over the North American area shown
804 is 0.65 or higher (roughly 2/3 of variance explained by the averaged field). b. Average of
805 the computed 250-mb eddy streamfunction fields over the nine experiments that examine
806 heating within the region enclosed by heavy dotted lines in (a). c. Square of the spatial
807 correlation (r^2) between each experiment's 250-mb eddy streamfunction field (from the

808 SWM analysis) and the 9-experiment average in (b). The value for a given experiment is
809 plotted within the corresponding box in the figure.

810 Figure 5. a. Percentile of average July soil moisture content in the different AGCM experiments,
811 with rankings based on the full ensemble of control simulations. The percentile shown
812 for a given grid cell is for the experiment in which that grid cell (along with its neighbors
813 within the marked box) was forced to be dry during April through June; the map is thus a
814 composite of results from different AGCM experiments. b. Difference (experiment
815 minus control) in the June through July evaporation computed in the AGCM
816 experiments. As in (a), the map shown is a composite; the difference shown for a given
817 grid cell is for the experiment in which that grid cell (along with its neighbors within the
818 marked box) was forced to be dry during April through June.

819 Figure 6. a. Anomalies ($10^6 \text{ m}^2/\text{s}$) in June-July 250-mb streamfunction (experiment minus
820 control) for Experiment AGCM-S. The imposed dryness in Region S has induced a
821 wavelike pattern in the streamfunction field. b. Same, but for June-July precipitation
822 anomalies (mm/day). c. Same, but for June-July 2-m air temperature anomalies ($^{\circ}\text{K}$).

823 Figure 7. a. Anomalies in June-July 250-mb streamfunction (experiment minus control) for
824 Experiment A. Significance levels (according to a t-test) are shown as contours, with
825 solid black for the 95% confidence level, dotted for the 99% confidence level, and solid
826 white for the 99.9% confidence level. b-u: Same, but for Experiments B-U. The heavy
827 red line encloses the experiments corresponding to the continental interior region
828 demarcated in Figure 4a.

829 Figure 8. Same as Figure 7, but for precipitation anomalies (mm/day).

830 Figure 9. Same as Figure 7, but for 2-m air temperature anomalies ($^{\circ}\text{K}$).

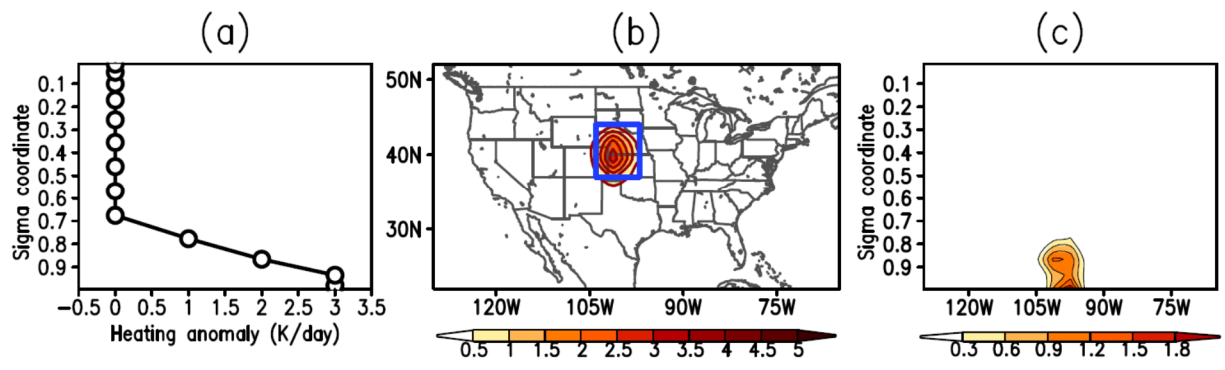
831 Figure 10. a. Composited field of 250-mb streamfunction anomalies from the ECMWF ERA-
832 Interim reanalysis, built from the 10% of the 210 June and July decads during 1980-2014
833 with the driest antecedent (15 day lead) continental soil moistures in the region indicated.
834 b. Same, but for MERRA-2 rain-gauge corrected precipitation. c. Same, but for ERA-
835 Interim 2-m air temperatures. d. Average of the June-July 250-mb eddy streamfunction
836 anomalies produced in the 9 SWM experiments indicated. e. Sum of the June-July 250-
837 mb streamfunction anomalies produced in the 9 AGCM experiments indicated. f. Same,
838 but for precipitation. g. Same, but for 2-m air temperature.

839 Figure 11. a. Number of $1^{\circ}\times 1^{\circ}$ grid cells across the indicated region (130W-60W, 20N-70N) for
840 which precipitation is modified at the 99% confidence interval by the dryness imposed in
841 each experiment. (The number of grid cells affected in a given experiment is plotted
842 within the dryness region associated with that experiment.) Gray shading indicates very
843 roughly the number expected by chance. b. Same, but for 2-m air temperature.

844 Figure 12. a. For each $1^{\circ}\times 1^{\circ}$ grid cell, the number of dryness regions (as outlined in the heavy
845 black lines) that, in our experiments, induce precipitation anomalies significant at the
846 99% confidence level. b. Same, but for 2-m air temperature.

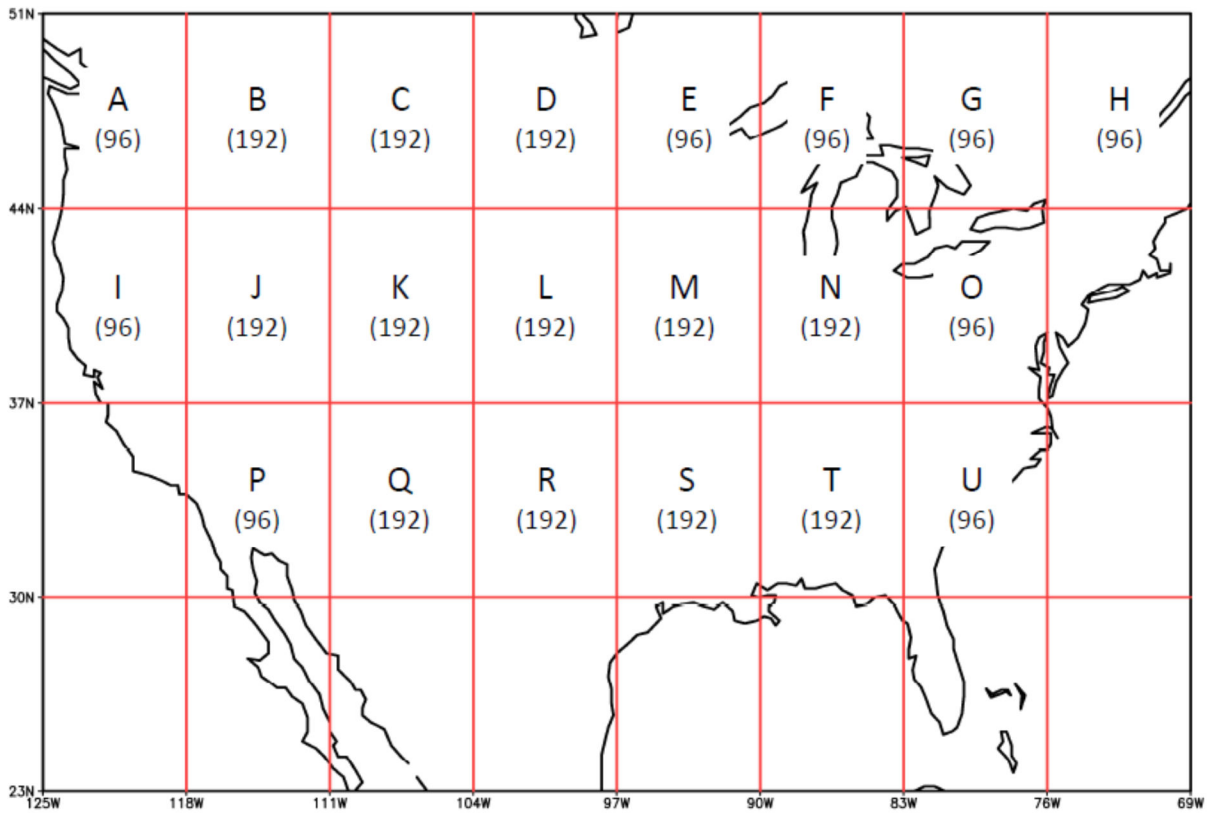
847 Figure 13. Schematic of a potential feedback loop suggested by the AGCM results. The dry soil
848 moistures induce (1) a specific circulation pattern that in turn induces (2) additional
849 warming and drying over the central US. This in turn leads (3) to higher sensible heat
850 fluxes from the land surface in the central US, which can enhance (4) the atmospheric
851 circulation anomaly that originally produced the warming and drying.

852
853
854
855
856
857
858
859



860
861

862 Figure 1. a. Vertical profile of idealized diabatic heating anomaly imposed in the SWM
863 atmosphere over a selected geographical area. b. Spatial distribution of imposed idealized
864 heating anomaly near the ground surface ($\sigma = 0.9966$), for experiment SWM-L. c. Vertical and
865 zonal structure of the ensemble mean June-July diabatic heating anomalies produced in
866 Experiment AGCM-L, averaged between 37°N and 44°N. Units: K/day.



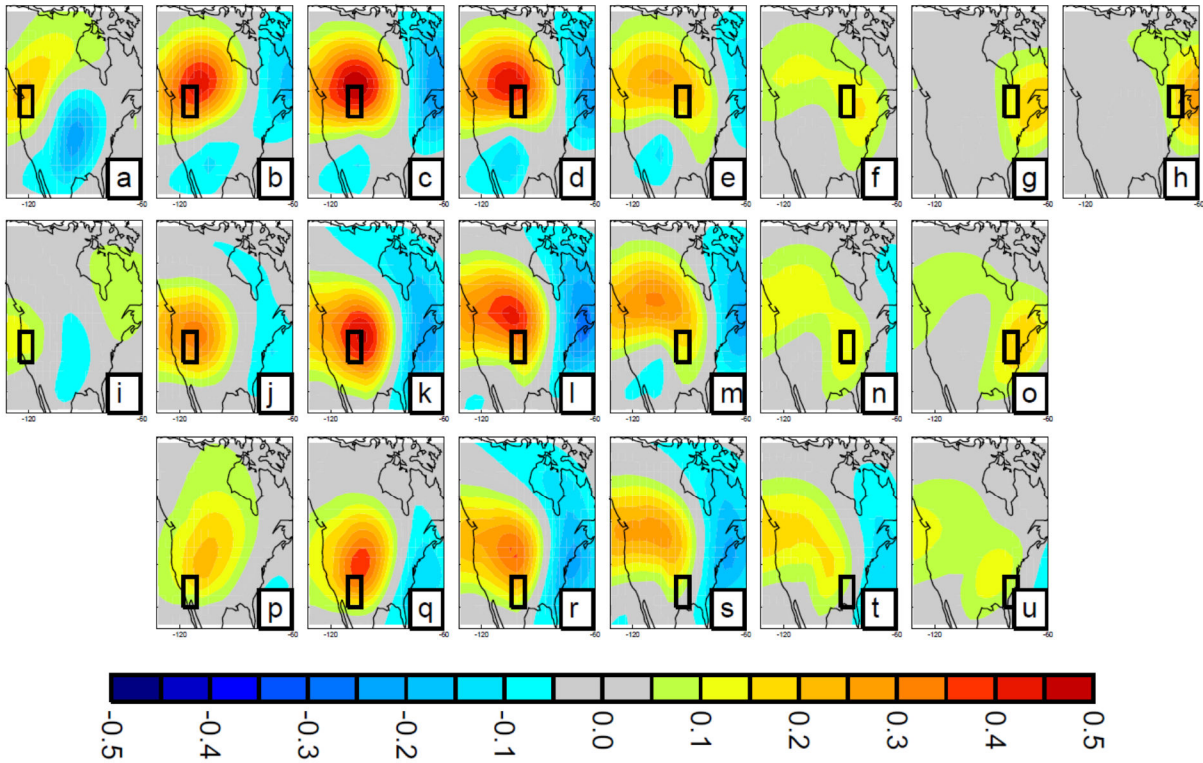
868

869

870 Figure 2. Areas of imposed dryness considered in the 21 SWM and AGCM experiments (labeled
 871 A through U). In a given AGCM experiment, the indicated region was forced to be dry through
 872 the artificial zeroing of the incident precipitation in April through June. The number of AGCM
 873 ensemble members associated with each experiment is indicated in parentheses.

874

SWM Results: Eddy Streamfunction ($10^6 \text{ m}^2/\text{s}$)



875

876

877

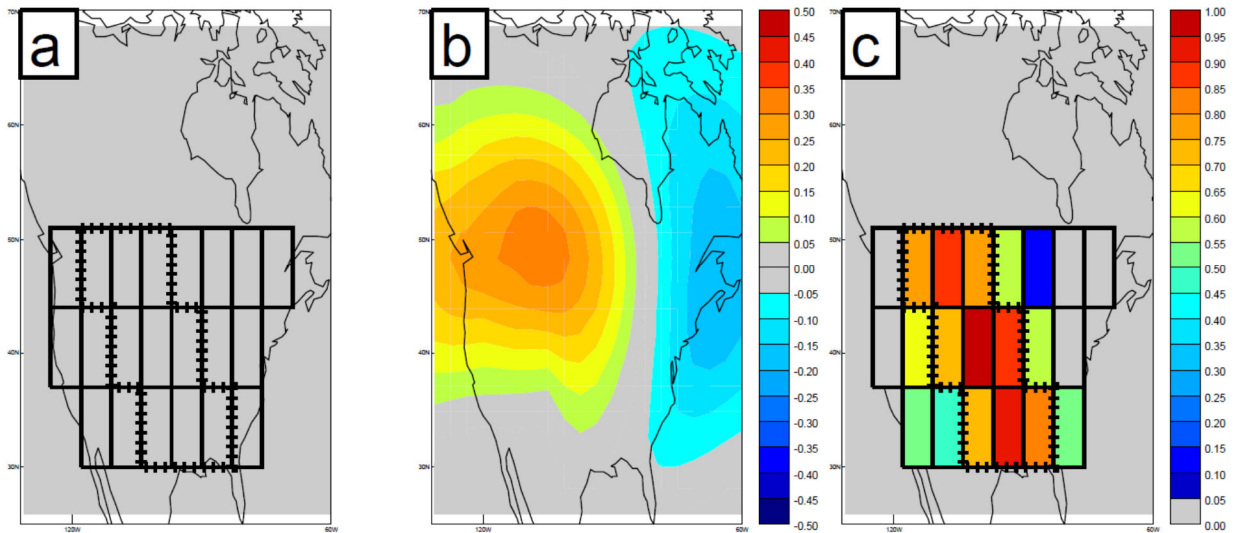
878 Figure 3. Eddy streamfunction anomaly fields at 250 mb produced in the SWM experiments.

879 The boxes indicate the locations for which the idealized diabatic heating source is placed.

880

881

882



883

884

885

886 Figure 4. Indication of the similarity between the 250-mb eddy streamfunction responses in the
887 different SWM experiments. a. Location of the 9 experimental regions for which the square of
888 the spatial correlation between the experiment's 250-mb eddy streamfunction field and the
889 average field over all 21 experiments over the North American area shown is 0.65 or higher
890 (roughly 2/3 of variance explained by the averaged field). b. Average of the computed 250-mb
891 eddy streamfunction fields ($10^6 \text{ m}^2/\text{s}$) over the nine experiments that examine heating within the
892 region enclosed by heavy dotted lines in (a). c. Square of the spatial correlation (r^2) between
893 each experiment's 250-mb eddy streamfunction field (from the SWM analysis) and the 9-
894 experiment average in (b). The value for a given experiment is plotted within the corresponding
895 box in the figure.

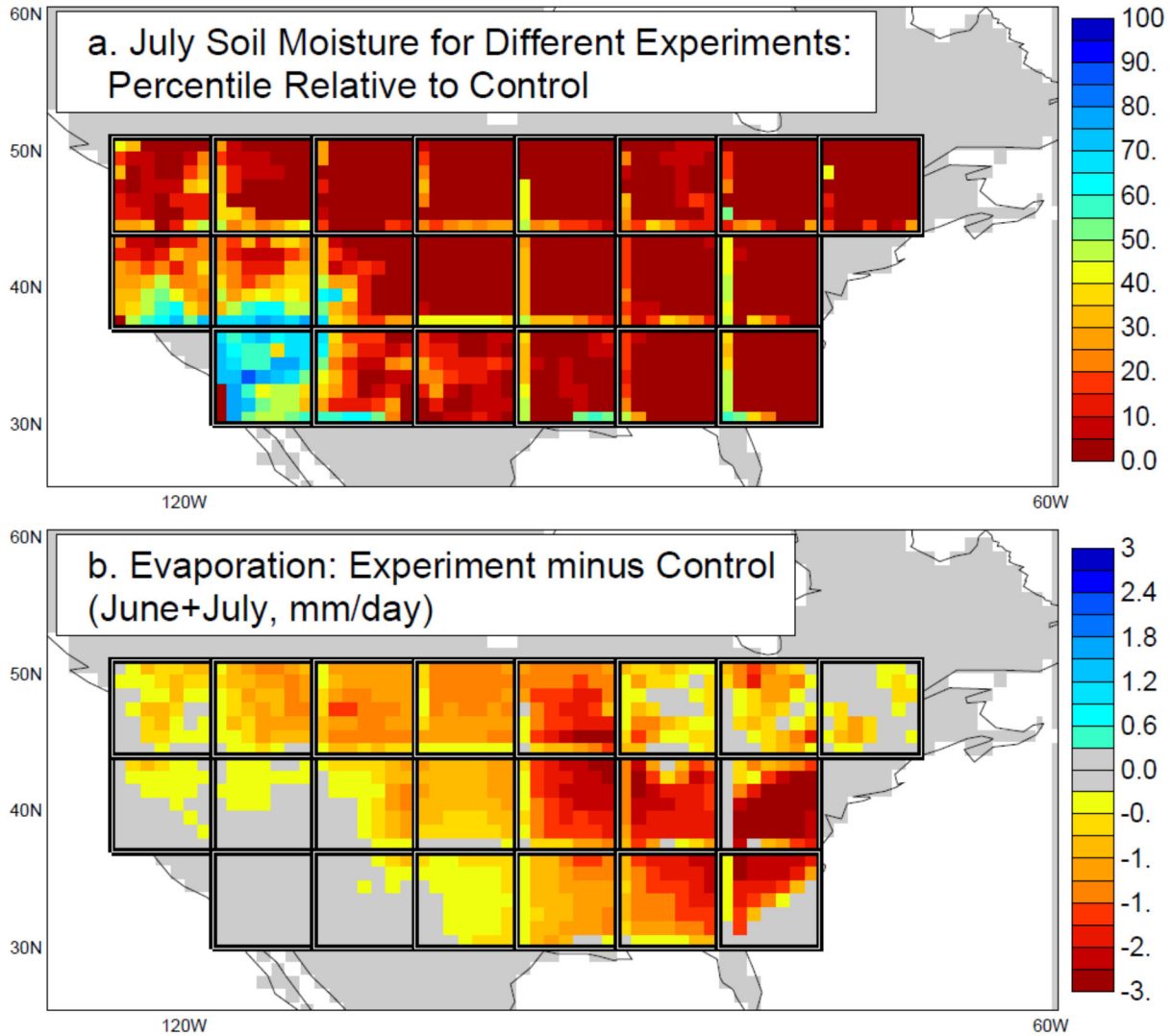
896

897

898

899

900



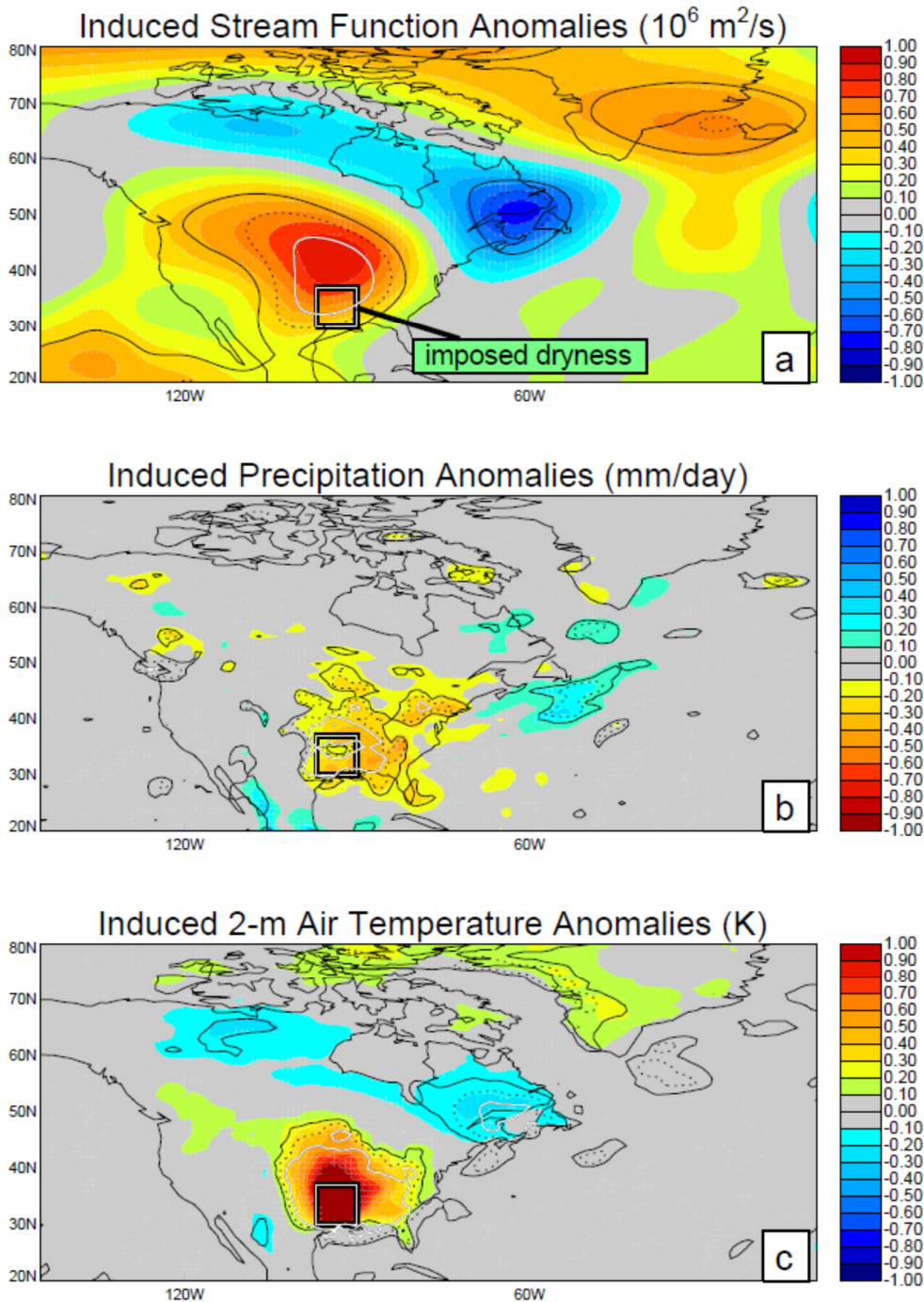
901

902

903

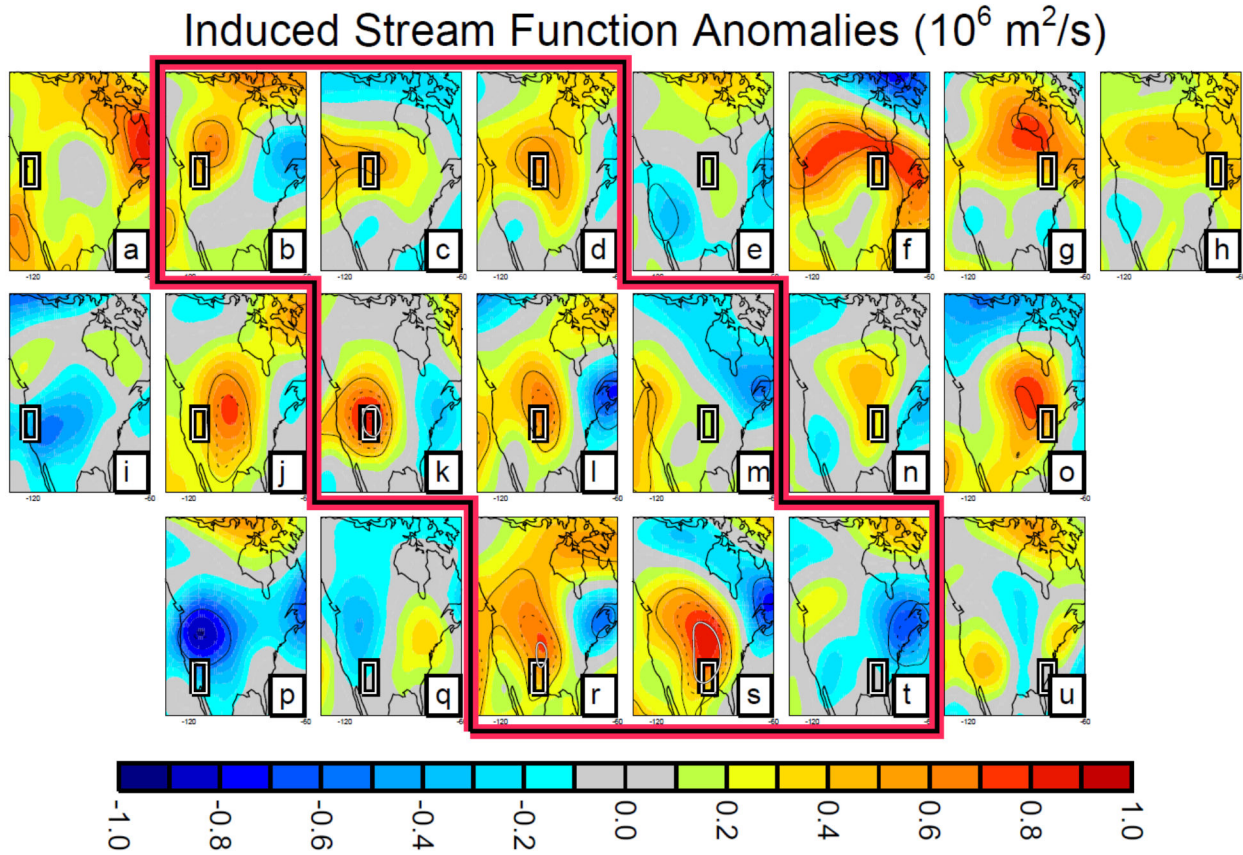
904 Figure 5. a. Percentile of average July soil moisture content in the different AGCM experiments,
905 with rankings based on the full ensemble of control simulations. The percentile shown for a
906 given grid cell is for the experiment in which that grid cell (along with its neighbors within the
907 marked box) was forced to be dry during April through June; the map is thus a composite of
908 results from different AGCM experiments. b. Difference (experiment minus control) in the June
909 through July evaporation computed in the AGCM experiments. As in (a), the map shown is a
910 composite; the difference shown for a given grid cell is for the experiment in which that grid cell
911 (along with its neighbors within the marked box) was forced to be dry during April through June.

912



915 Figure 6. a. Anomalies ($10^6 \text{ m}^2/\text{s}$) in June-July 250-mb streamfunction (experiment minus
 916 control) for Experiment AGCM-S. Significance levels (according to a t-test) are shown as
 917 contours, with solid black for the 95% confidence level, dotted for the 99% confidence level,
 918 and solid white for the 99.9% confidence level. The imposed dryness in Region S has induced a
 919 wavelike pattern in the streamfunction field. b. Same, but for June-July precipitation anomalies
 920 (mm/day). c. Same, but for June-July 2-m air temperature anomalies ($^{\circ}\text{K}$).

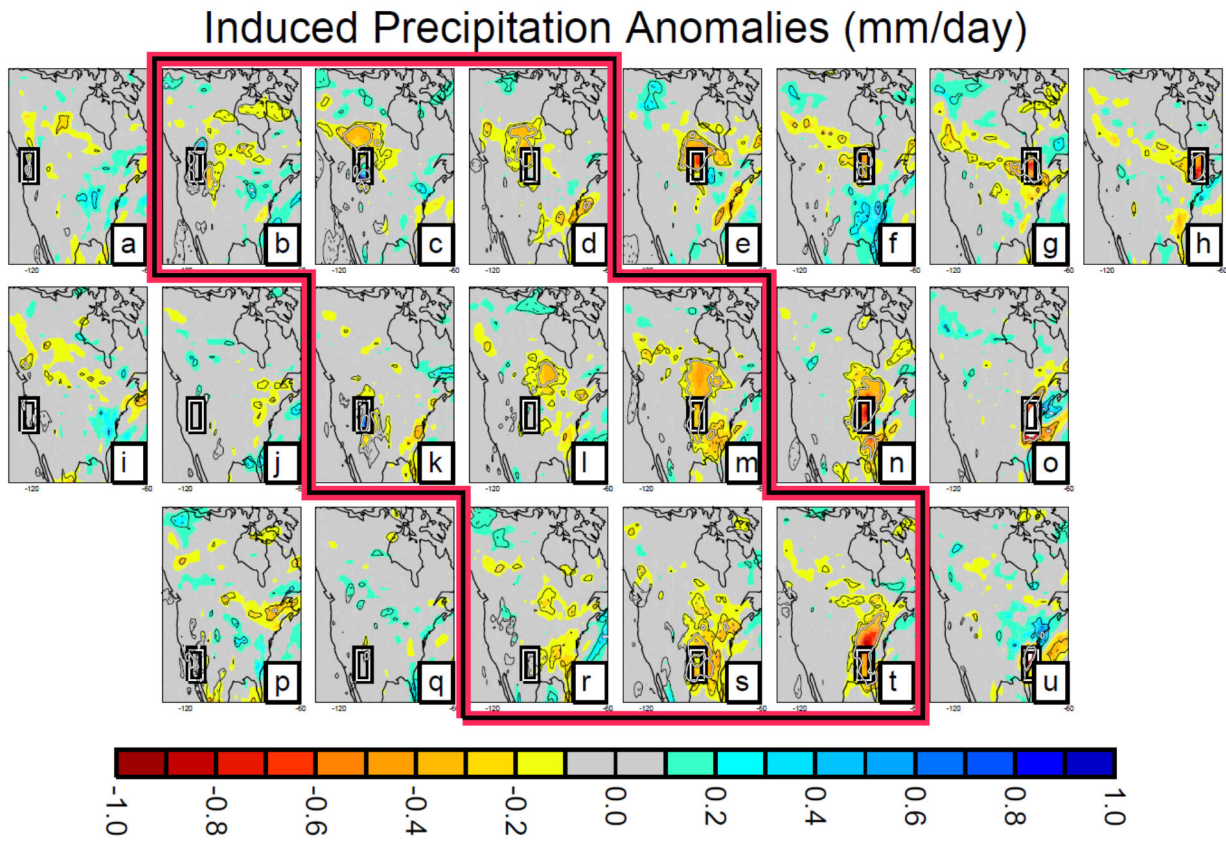
921
922
923



924
925
926
927

928 Figure 7. a. Anomalies in June-July 250-mb streamfunction (experiment minus control) for
929 Experiment A. Significance levels (according to a t-test) are shown as contours, with solid black
930 for the 95% confidence level, dotted for the 99% confidence level, and solid white for the 99.9%
931 confidence level. b-u: Same, but for Experiments B-U. The heavy red line encloses the
932 experiments corresponding to the continental interior region demarcated in Figure 4a.

933
934
935
936

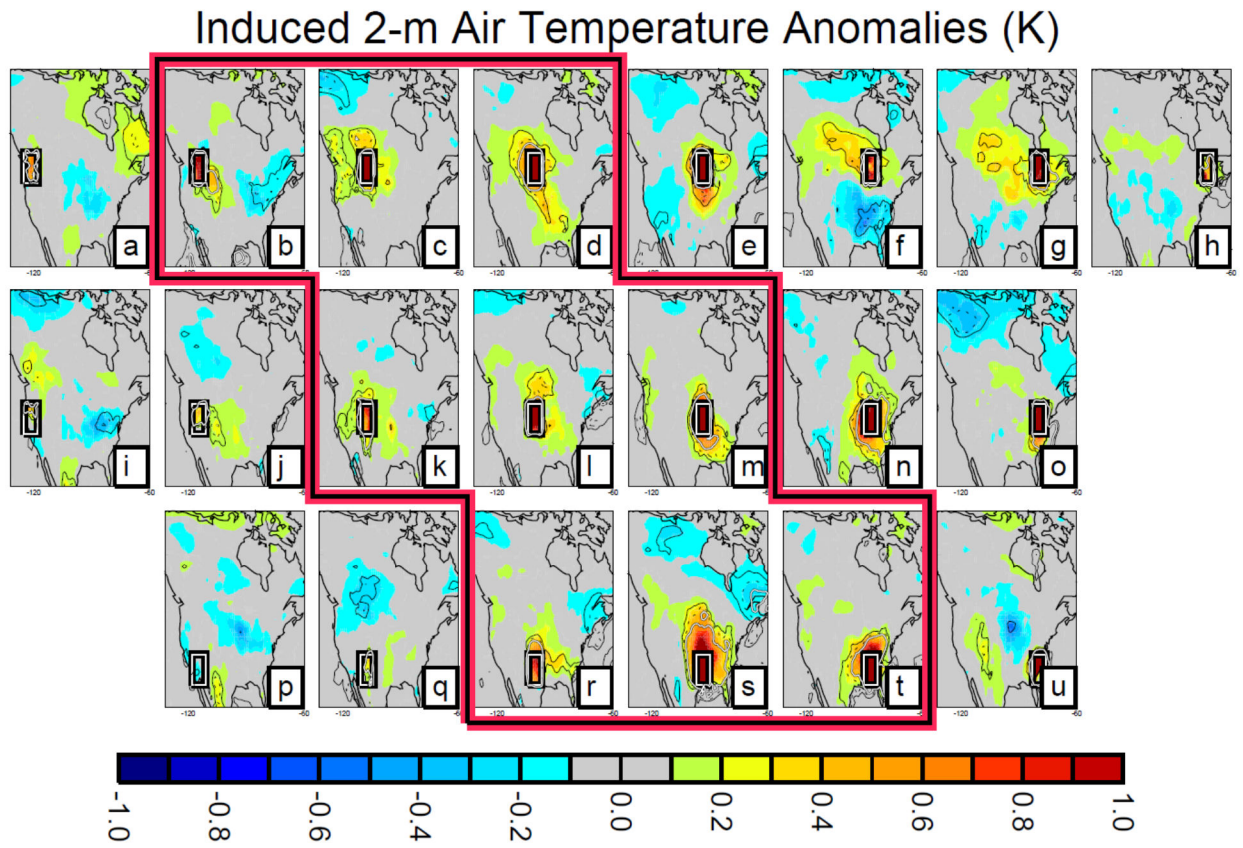


937
938
939
940

Figure 8. Same as Figure 7, but for precipitation anomalies (mm/day).

941

942

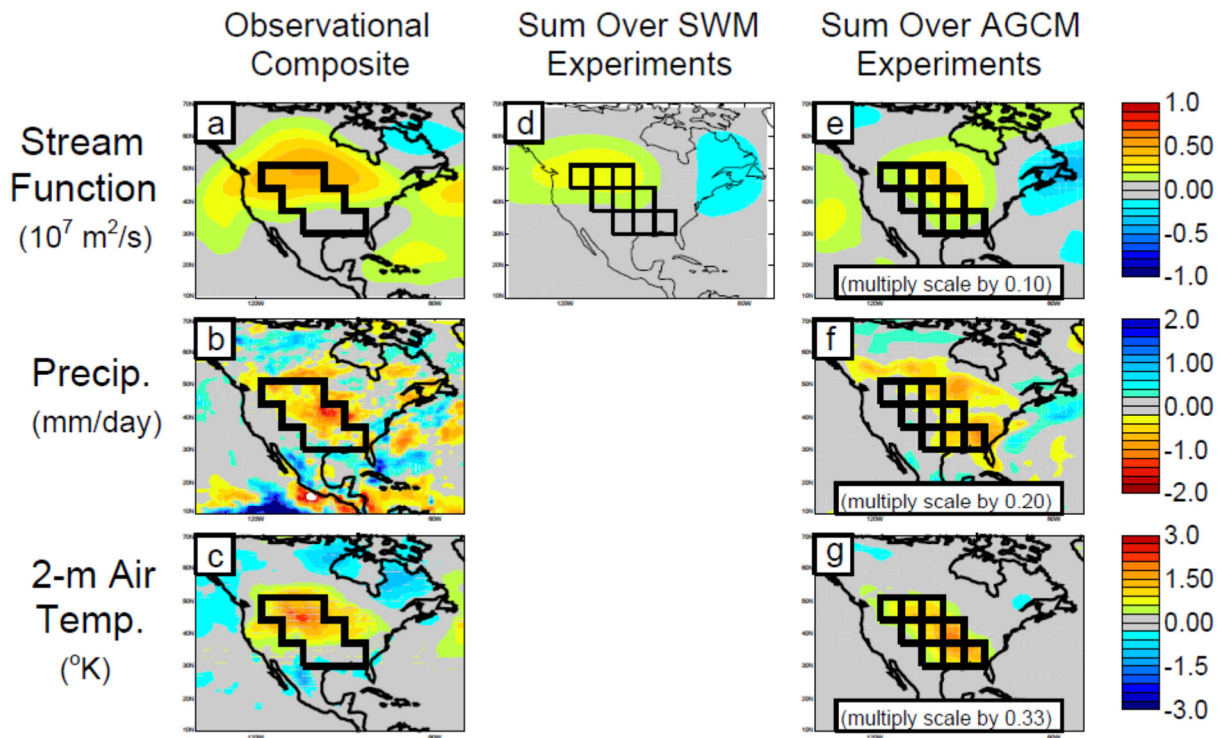


943

944

945 Figure 9. Same as Figure 7, but for 2-m air temperature anomalies ($^{\circ}$ K).

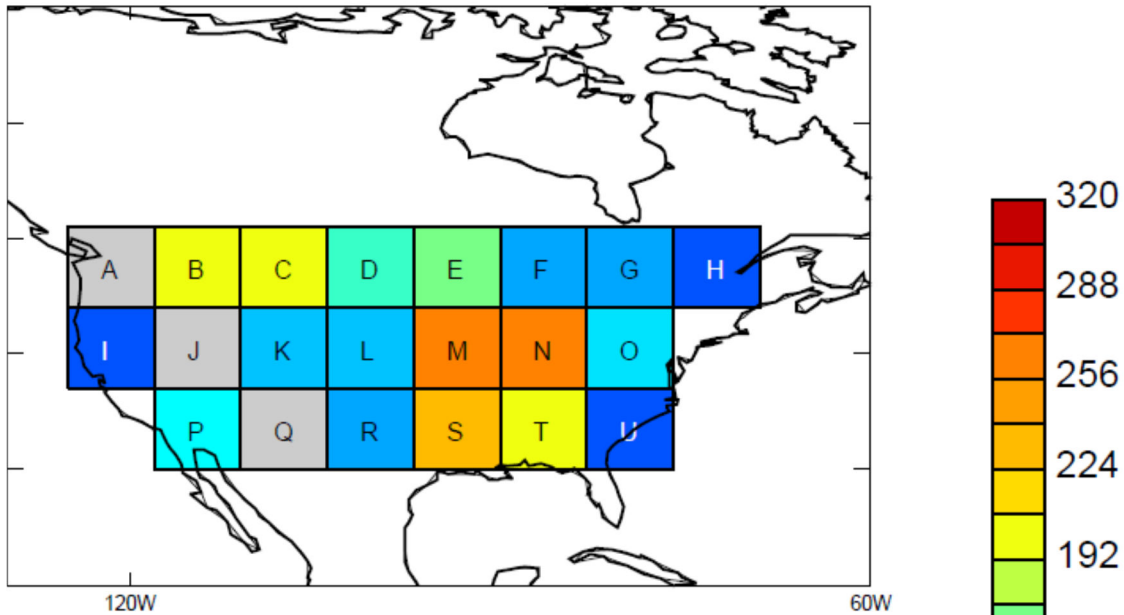
946
947
948
949
950



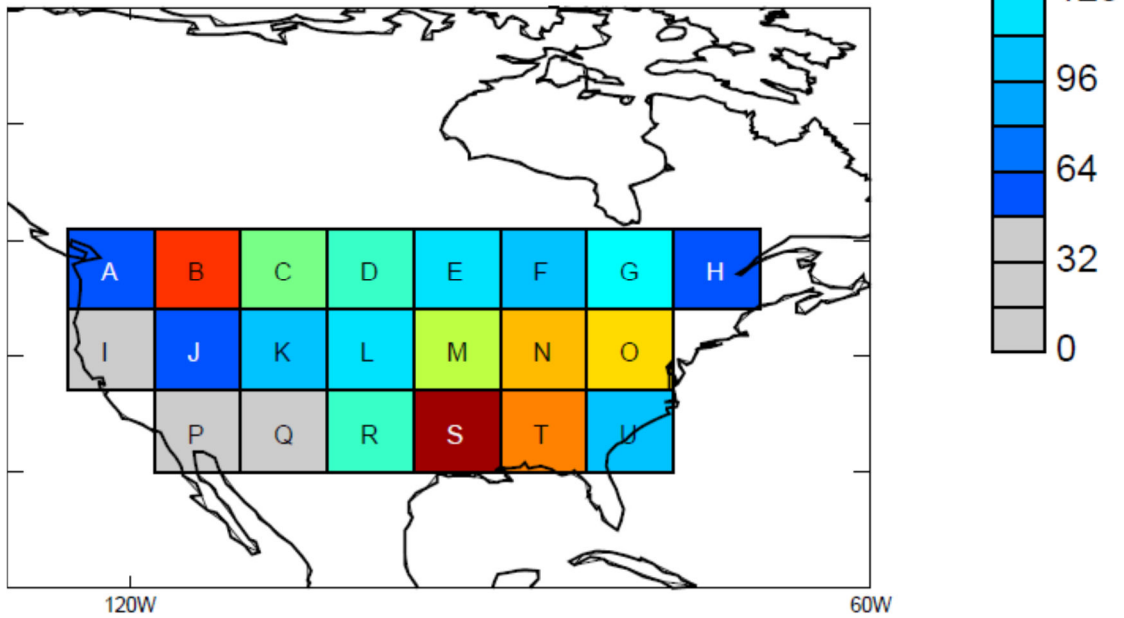
951
952
953
954
955
956
957
958
959
960
961
962
963

Figure 10. a. Compositing field of 250-mb streamfunction anomalies from the ECMWF ERA-Interim reanalysis, built from the 10% of the 210 June and July decads during 1980-2014 with the driest antecedent (15 day lead) continental soil moistures in the region indicated. b. Same, but for MERRA-2 rain-gauge corrected precipitation. c. Same, but for ERA-Interim 2-m air temperatures. d. Average of the June-July 250-mb eddy streamfunction anomalies produced in the 9 SWM experiments indicated. e. Sum of the June-July 250-mb streamfunction anomalies produced in the 9 AGCM experiments indicated. f. Same, but for precipitation. g. Same, but for 2-m air temperature.

a. Prec: # cells affected at 99% confidence level by source



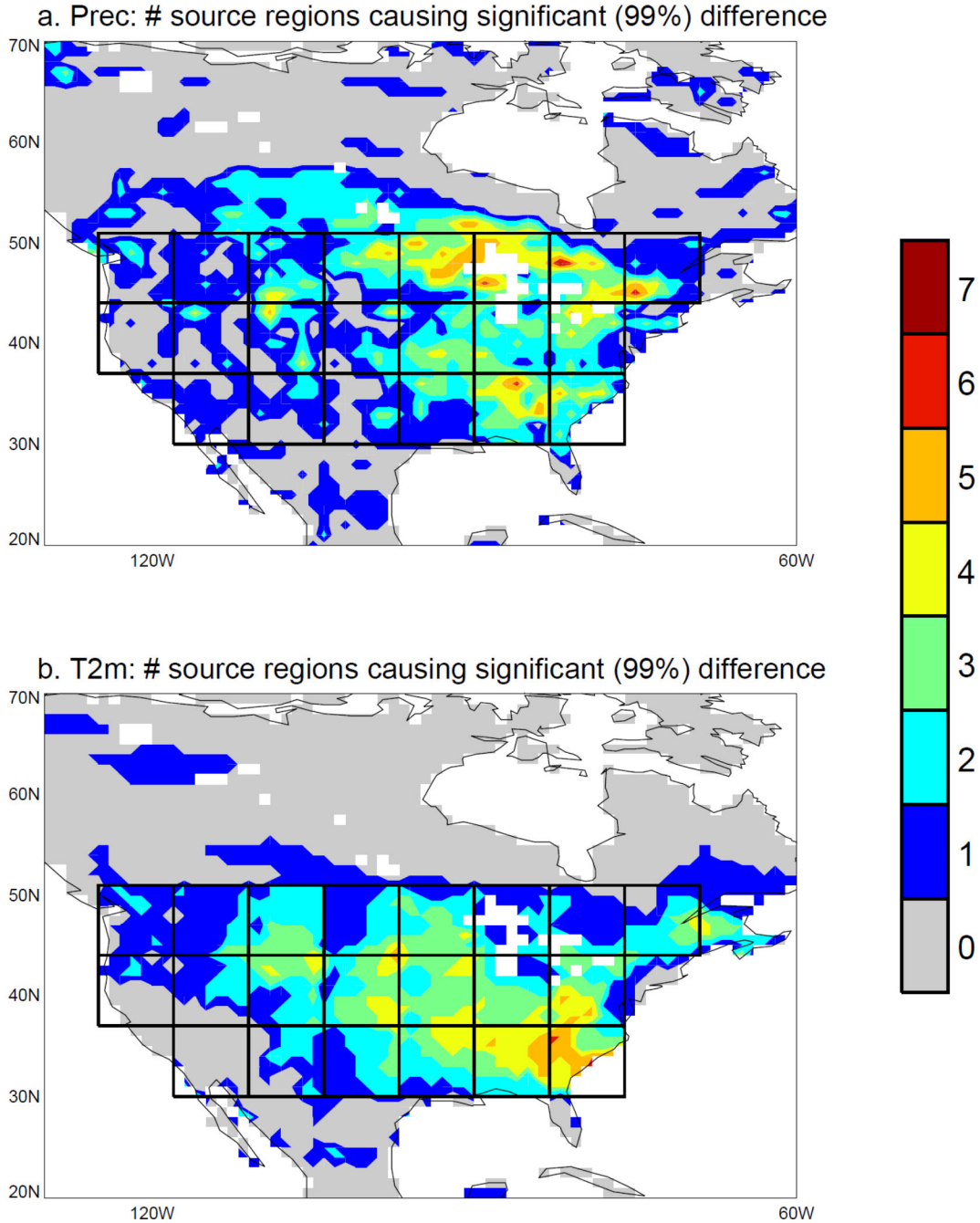
b. T2m: # cells affected at 99% confidence level by source



964

965

966 Figure 11. a. Number of 1°×1° grid cells across the indicated region (130W-60W, 20N-70N, or
 967 3621 cells) for which precipitation is modified at the 99% confidence interval by the dryness
 968 imposed in each experiment. (The number of grid cells affected in a given experiment is plotted
 969 within the dryness region associated with that experiment.) Gray shading indicates very roughly
 970 the number expected by chance. b. Same, but for 2-m air temperature.

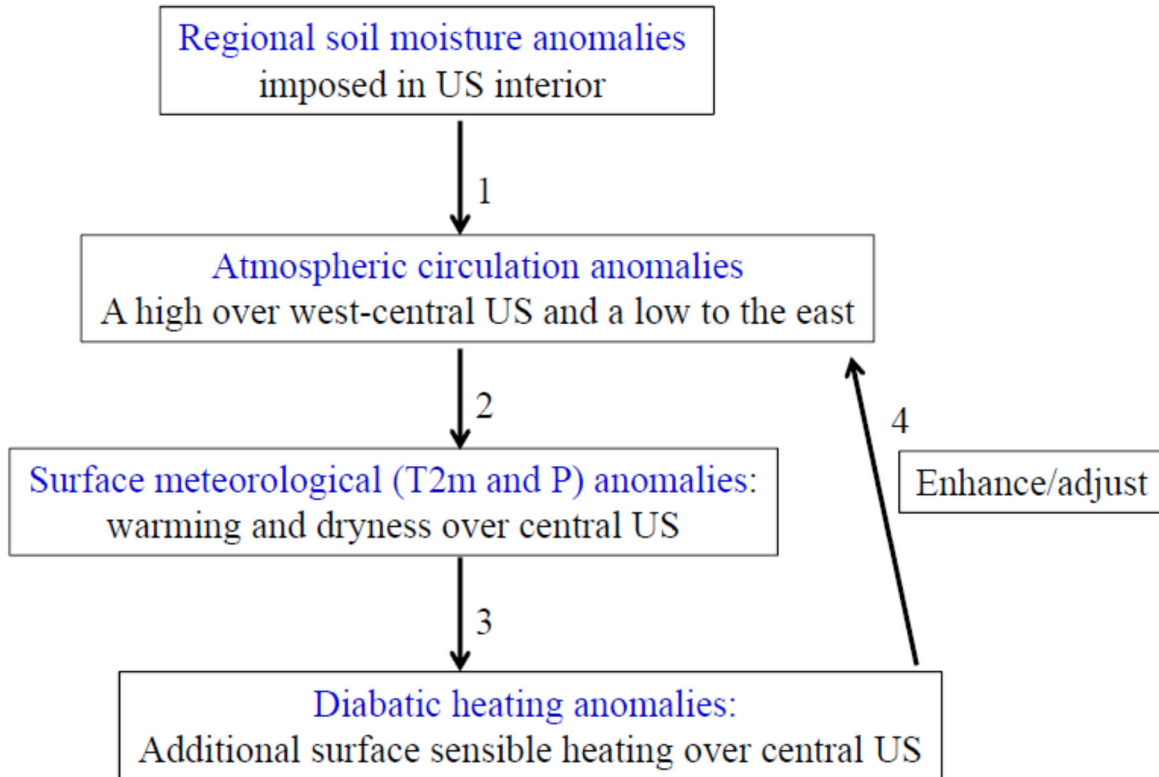


971

972

973 Figure 12. a. For each $1^\circ \times 1^\circ$ grid cell, the number of dryness regions (as outlined in the heavy
 974 black lines) that, in our experiments, induce precipitation anomalies significant at the 99%
 975 confidence level. b. Same, but for 2-m air temperature.

976



977

978

979 Figure 13. Schematic of a potential feedback loop suggested by the AGCM results. The dry soil
 980 moistures induce (1) a specific circulation pattern that in turn induces (2) additional warming and
 981 drying over the central US. This in turn leads (3) to higher sensible heat fluxes from the land
 982 surface in the central US, which can enhance (4) the atmospheric circulation anomaly that
 983 originally produced the warming and drying.

984